

Vrije Universiteit Brussel



Faculteit Wetenschappen  
Departement Natuurkunde

# **Measurement of the $W$ helicities in top quark events with CMS**

**Annik Olbrechts**

Promotor: Prof. Dr. Jorgen D'Hondt  
Academiejaar: 2010 – 2011

Proefschrift ingediend met het oog op het behalen  
van de academische graad Master in de Fysica

# Contents

<b>Introduction</b>	<b>iii</b>
<b>Dankwoord</b>	<b>v</b>
<b>1 Top Quark Physics in the Standard Model</b>	<b>1</b>
1.1 The Standard Model . . . . .	1
1.1.1 Particle content and interactions . . . . .	1
1.1.2 Mathematical framework of the Standard Model . . . . .	3
1.1.3 Open questions . . . . .	4
1.2 Top Quark physics . . . . .	6
1.3 Phenomenology of the Wtb coupling . . . . .	8
1.3.1 Weak Charged Current and V-A structure . . . . .	8
1.3.2 The CKM matrix . . . . .	10
1.3.3 Measuring W helicities . . . . .	12
<b>2 The CMS Experiment at the LHC</b>	<b>13</b>
2.1 The Large Hadron Collider . . . . .	13
2.1.1 Experiments at the LHC . . . . .	15
2.2 The Compact Muon Solenoid . . . . .	16
2.2.1 The Silicon Tracker . . . . .	18
2.2.2 The Electromagnetic Calorimeter . . . . .	18
2.2.3 The Hadronic Calorimeter . . . . .	19
2.2.4 The Muon System . . . . .	20
2.2.5 The Trigger System . . . . .	21
2.3 Simulating proton collisions . . . . .	22
2.4 Data taking in 2010 . . . . .	22
<b>3 Reconstruction of top-pair events</b>	<b>25</b>
3.1 Jet Reconstruction . . . . .	25
3.2 Muon Reconstruction . . . . .	28
3.3 b-flavour Identification . . . . .	30

---

3.4	Missing Energy . . . . .	33
<b>4</b>	<b>Selecting top-pair topologies</b>	<b>37</b>
4.1	Event Selection . . . . .	37
4.2	Jet-quark matching algorithm . . . . .	44
<b>5</b>	<b>Helicity distribution reconstruction</b>	<b>48</b>
5.1	Differential cross section and helicities . . . . .	48
5.2	Reweighting expected helicity distribution . . . . .	55
5.3	Application of b-tagging . . . . .	56
<b>6</b>	<b>Measurement on 2010 data</b>	<b>62</b>
6.1	Helicity Measurement . . . . .	62
6.2	Systematic Uncertainties . . . . .	65
6.2.1	Variation of Jet Energy Scale . . . . .	65
6.2.2	Variation of W Cross Section . . . . .	66
6.2.3	Effect of Background Processes . . . . .	67
<b>7</b>	<b>Conclusions and Outlook</b>	<b>70</b>
	<b>Summary</b>	<b>73</b>
	<b>Samenvatting</b>	<b>75</b>

# Introduction

Since 1960 the Standard Model of particle physics describes the elementary particles and interactions and all observations obtain excellent agreement. Hence the Standard Model is considered as a very successful theory to understand Nature. With the discovery of the top quark in 1995, the heaviest quark in the Standard Model, the Standard Model was considered to be complete. Hence the search towards indications of physics beyond the Standard Model started.

For this search the top quark is essential due to his high mass, about 50 times larger than the bottom quark. Because the high mass of the top quark it is expected to be the most sensitive to new physics influences. Therefore an accurate knowledge of the properties of the top quark will result in information about new physics phenomena.

The subject of this thesis is the measurement of the helicity of the W-boson produced in the decay of the top quark. Due to the short lifetime of the top quark, a direct consequence of its high mass, the top quark is the only quark in the Standard Model which can be studied as a bare quark, free from hadronization effects. Hence the spin information is not lost, making a measurement of the W-boson helicity possible.

The Standard Model predicts the helicity of the W-bosons to be either negative or zero, but not positive. In case the top quark sector is influenced by new physics phenomena the V-A structure of the weak charged current interaction, which is responsible for the decay of the top quark, can be altered. Since the helicity of the W-bosons has an influence on the angular distribution of its decay products, any deviation from the Standard Model will be visible in the distribution of the decay angle  $\theta^*$  between the lepton in the W-boson restframe and the W-boson in the top quark restframe.

In the first chapter a general overview of the Standard Model and Top Quark physics is given. The theoretical framework of the Wtb coupling is described in detail. This thesis makes use of proton-proton collisions pro-

---

duced at the CERN Large Hadron Collider and recorded with the Compact Muon Solenoid detector. The characteristics of this detector and its various subdetectors is given in chapter two. In this thesis semi-muonic decaying top pair events are used to measure the W-boson helicities. Hence the expected signal in the CMS detector consists of two light jets, two b-quark jets, one muon and missing energy representing the neutrino. Chapter three explains how these physics objects are reconstructed with the CMS detector. In the fourth chapter the event selection to reduce the background and select the correct event topology is described together with the used method to match the measured jets with the quarks in the events. In the fifth chapter the followed analysis method is presented. The background contamination of the data sample is reduced using b-quark identification. Chapter six gives the obtained measurement together with the detailed study of systematic uncertainties, potentially affecting the measurement. In the seventh and final chapter the result is summarized and an outlook of the expected achievable precision with this analysis on the increasing amount of data available at the Large Hadron Collider.

# Dankwoord

Eerst en vooral dank aan mijn promotor, Prof. Dr. Jorgen D'Hondt, voor de vele tijd en moeite die hij in mijn thesis heeft geïnvesteerd. Zonder zijn begeleiding had ik deze analyse nooit tot een goed einde kunnen brengen. Ook het inzicht dat ik reeds heb gewonnen over onderzoek in de experimentele deeltjesfysica heb ik volledig aan hem te danken.

Verder wil ik ook de doctoraatstudenten en post-docs in het *Top Quark Team* bedanken, voornamelijk Stijn en Michael, die steeds bereid waren uitleg en advies te geven.

Ook wil ik graag mijn bureaugenoot Jan en andere klasgenoten bedanken voor de vele interessante discussies, binnen en buiten de Fysica.

Ten slotte wil ik mijn ouders bedanken die mij de kans hebben gegeven om fysica te studeren en die mij altijd zijn blijven steunen om mijn studies tot een goed einde te brengen.

# Chapter 1

## Top Quark Physics in the Standard Model

Elementary particle physics is the branch of physics where one tries to understand the smallest constituents of matter. For almost forty years the Standard Model of Particle physics describes all the known experimental facts about elementary particle physics. It incorporates the electromagnetic, weak and strong interactions but not gravity. The excellent experimental match indicates that the Standard Model is a very successful and precise theory. Current research with the Compact Muon Solenoid (CMS) detector located at the Large Hadron Collider (LHC) at CERN near Geneva mainly probes into physics beyond the Standard Model.

The Standard Model was completed in 1995 with the discovery of the top quark, the most heavy and final missing particle. After this, the search towards extensions of the Standard Model started.

### 1.1 The Standard Model

The Standard Model of Particle Physics, a gauge theory which is mathematically described by the symmetry group  $SU(3)_C \otimes SU(2)_L \otimes U(1)_Y$ , represents the strong, weak and electromagnetic interactions via the exchange of force-carrier particles.

#### 1.1.1 Particle content and interactions

The Standard Model contains two different classes of particles which can be distinguished by their spin. The first kind are called fermions and have half-integer spin while the second kind are called bosons and have integer spin.

They are considered respectively as the elementary building blocks and the force-mediators of the universe.

The 12 fermions all have an anti-particle with the same mass but opposite electric charge and are organized into a three-fold family structure as shown in Table (1.1). The fermions can be arranged into generations since the particles in each generation have almost identical properties, except for their mass. The mass of the particles increases for each generation allowing the decay into lower-generation particles. Therefore all ordinary matter is build from the generally stable first generation. The atoms of all chemical elements consist of electrons surrounding a nucleus of protons and neutrons which are a combination of up and down quarks.

The fermions can further be divided into quarks and leptons, based on the allowed interactions. Quarks possess electric charge, color charge and weak isospin and therefore interact through the electromagnetic, strong and weak force respectively. Leptons are insensitive to the strong force and the uncharged leptons only interact through the weak interaction making them very difficult to detect.

	Charge	1 <sup>st</sup> Generation		2 <sup>nd</sup> Generation		3 <sup>rd</sup> Generation	
<b>Quarks</b>	+2/3	Up	u	Charm	c	Top	t
	-1/3	Down	d	Strange	s	Bottom	b
<b>Leptons</b>	0	Electron neutrino	$\nu_e$	Muon neutrino	$\nu_\mu$	Tau neutrino	$\nu_\tau$
	-1	Electron	$e^-$	Muon	$\mu^-$	Tau	$\tau^-$

**Table 1.1:** Organization of fermions in the Standard Model.

In the Standard Model fundamental interactions are considered as being mediated by force-carriers or gauge bosons. The Standard Model holds 8 massless gluons, 1 massless photon and 3 massive bosons,  $W^\pm$  and  $Z^0$  for respectively the strong, electromagnetic and weak interaction as shown in Table (1.2). The graviton, responsible for the mediation of the gravitational force, is not included.

The strong interaction has the peculiar property that the force field strengthens for increasing distance. Therefore as two quarks separate, the gluon fields between them will not diminish but will form a narrow band holding them together and will finally split into a new quark-antiquark pair. As a result only color neutral bound states of quarks, called hadrons, can be observed.

Interaction	Boson	Mass (GeV/c <sup>2</sup> )	Quantum number
Electromagnetic	Photon $\gamma$	0	Electric charge Q
Weak interaction	$W^\pm$	$80.399 \pm 0.023$	Weak isospin $I_3$
	$Z^0$	$91.1876 \pm 0.0021$	
Strong	Gluon $g_{1,\dots,8}$	0	Color charge (r,g,b)

**Table 1.2:** Gauge bosons of the Standard Model and their masses [1] and quantum numbers. The photon and gluon masses are the theoretical predictions.

### 1.1.2 Mathematical framework of the Standard Model

The Standard Model is mathematically described by a relativistic quantum field theory with local gauge invariance [3, 4]. This implies that the equations of motion can be obtained with Hamilton's variational principle of least action as in classical mechanics. The action is defined as  $S = \int \mathcal{L} d^4x$  where the Lagrangian density  $\mathcal{L}$  only depends on the particle's wave function  $\psi(x)$  and its derivative  $\partial^\mu \psi(x)$ . Using Hamilton's principle the equations of motion, or Euler-Lagrange equations, can be obtained by demanding that the action has a stationary value for variations of the fields  $\delta S = 0$ .

The spin 1/2 fermions of the Standard Model are represented by Dirac spinors  $\psi(x)$  and the Dirac Lagrangian  $\mathcal{L}^{Dirac}$ . The  $4 \times 4$  gamma- or Dirac-matrices  $\gamma^\mu$  satisfy  $\{\gamma^\mu, \gamma^\nu\} = 2\eta^{\mu\nu}$  and  $(\gamma^\mu)^\dagger = \gamma^0 \gamma^\mu \gamma^0$ .

$$\mathcal{L}^{Dirac} = i\bar{\psi}\gamma^\mu\partial_\mu\psi - m\bar{\psi}\psi \quad (1.1)$$

The Lagrangian density in Equation (1.1) is the free-fermion Lagrangian density without interacting fields. In order to include fermion-field interactions the successful non-relativistic quantum mechanical procedure of minimal substitution should be adopted:

$$i\hbar\frac{\partial}{\partial t} \rightarrow i\hbar\frac{\partial}{\partial t} - q\phi(x), \quad -i\hbar\nabla \rightarrow -i\hbar\nabla - \frac{q}{c}\mathbf{A}(x) \quad (1.2)$$

In terms of the four-vector potential  $A^\mu(x) = (\phi, \mathbf{A})$  this substitution corresponds to interchanging the partial derivative in (1.1) with the covariant derivative in (1.3). This procedure ensures that the Lagrangian density is invariant under local phase transformations, which can be represented in terms of rotation parameters  $\alpha_j(x)$  and generators of the corresponding Lie group  $\sigma_j$ , as shown in Equation (1.4). Hence the effect of the partial derivative

acting on the functions  $\alpha_j(x)$  gets canceled out by the second term of the covariant derivative, which restores invariance.

$$\mathcal{D}_\mu = \partial_\mu - ig \frac{\vec{\sigma}}{2} \cdot \vec{A}_\mu \quad (1.3)$$

$$\psi'(x) = U(x)\psi(x) = e^{-ig\vec{\alpha}(x) \cdot \frac{\vec{\sigma}}{2}} \psi(x) \quad (1.4)$$

Finally the Dirac Lagrangian describing the coupling with strength  $g$  between the fermion field and the interacting vector field  $A_\mu^i$  is given in Equation (1.5). In order for this Lagrangian density to be gauge invariant the covariant derivative should transform in the same way as the field  $\psi(x)$  itself.

$$\begin{aligned} \mathcal{L}^{Dirac} &= i\bar{\psi}\gamma^\mu\mathcal{D}_\mu\psi - m\bar{\psi}\psi \\ &= i\bar{\psi}\gamma^\mu\partial_\mu\psi - m\bar{\psi}\psi - ig\bar{\psi}\gamma^\mu\frac{\vec{\sigma}}{2} \cdot \vec{A}_\mu\psi \end{aligned} \quad (1.5)$$

The Lagrangian density describing the Standard Model interactions can be obtained by considering  $SU(2)_L \times U(1)_Y$  and  $SU(3)_C$  local phase transformations for respectively the electroweak and strong interaction.

The subscript L for the Lie group  $SU(2)$  indicates that the  $SU(2)$  transformations only act on left-handed fermions<sup>1</sup>, as a consequence no mass term is allowed in the corresponding Lagrangian density. The mass of the fermions and weak gauge bosons is generated with the Brout-Englert-Higgs mechanism of spontaneous symmetry breaking.

The subscript Y stands for the hypercharge and distinguishes between the  $U(1)_{em}$  group which is retrieved after symmetry breaking. The color charge C avoids confusion with the  $SU(3)$  group describing the quarks (u,d,s) until 1970.

### 1.1.3 Open questions

The Standard Model is considered to be a very successful theory but is not accepted as a fundamental theory of particle physics because of the numerous shortcomings. The Higgs boson, unification of the forces, dark matter and energy and baryon asymmetry are the most important shortcomings and the main motivation for the Large Hadron Collider project which can probe fundamental interactions up to very high energies. Therefore it's possible to study indirectly the circumstances close to the Big Bang with high accuracy since the attainment of the top quark opens the door of the Terra world.

---

<sup>1</sup>Left-handed fermions are represented by  $\psi_L = \frac{1}{2}(1 - \gamma^5)\psi$  and right-handed by  $\psi_R = \frac{1}{2}(1 + \gamma^5)\psi$  with  $\gamma^5 = i\gamma^0\gamma^1\gamma^2\gamma^3$ . For more detail see section 1.3 .

The Higgs boson [5, 6] is a spin-0 particle postulated by R. Brout, F. Englert and P. W. Higgs in 1964 to explain the origin of the mass of fermions and weak gauge bosons. The major success of the proposed spontaneous symmetry breaking of  $SU(2)_L \times U(1)_Y$  into  $U(1)_{em}$ , at the electroweak breaking scale of 246 GeV [7], is the discovery of the  $W^\pm$  and  $Z^0$  boson with the predicted masses. The Higgs boson mass is not known which renders a possible identification more difficult, but the yet unexplored mass range is accessible for the Large Hadron Collider.

Ever since Maxwell postulated in 1873 the unification of electricity and magnetism into electromagnetism the search towards one unified force describing the four fundamental forces started. A first success was obtained in 1963 when Glashow, Salam and Weinberg proposed the partially unified electroweak interaction. Currently the unification of the electroweak and strong interaction is being investigated for which experiments indicate that the strengths of the forces comes close at high energies. A popular idea to explain such a unification is supersymmetry or SUSY [8], a Standard Model extension which introduces for each particle a supersymmetric partner differing by half a unit of spin. If SUSY exists these superpartners should appear in the proton collisions at the LHC.

All what is visible in the Universe only accounts for about 4% of its content, implying that most of the universe is made up of invisible substances, called dark matter (23%) and dark energy (76%), that do not emit electromagnetic radiation [9]. Hence their presence can only be detected through gravitational effects. Dark matter is responsible for galaxy formation while dark energy explains the expansion of the universe. Since the best candidates for dark matter are supersymmetric particles the LHC may shed some light on this topic.

The last major incompleteness of the Standard Model is the baryon asymmetry or absence of antimatter in the universe. As it is assumed that the universe is neutral with all conserved charges the Big Bang should have produced equal amounts of matter and antimatter [9]. Possible explanations of the observed discrepancy consist of CP violation in the weak interaction and the existence of separated matter- and antimatter-dominated regions in the universe. The LHC will study the matter versus antimatter comparison to identify possible subtle differences.

Finally the LHC, and especially the ALICE experiment, will study the possible existence of quark-gluon plasma since the current strong interaction

postulates that the confinement of the quarks and gluons vanishes at very high energies [9].

## 1.2 Top Quark physics

The top quark was postulated in 1973 by M. Kobayashi and T. Maskawa to complete the three-generation structure of the Standard Model and to explain the CP violation in kaon decay [10]. The large mass of the top quark, about 35 times heavier than the next heavy quark, retarded the discovery until 1995 by the CDF and DØ experiments of the Tevatron  $p\bar{p}$  collider at Fermilab [11]. The Tevatron was the first particle collider which could reach high enough energies to produce the heavy top quark, namely 1.8 TeV and 1.96 TeV during respectively Run-I and Run-II. Since the LHC has a centre-of-mass energy of 7 TeV, much higher than the 1.96 TeV Tevatron value, the LHC will become the main experiment measuring the top quark properties. The total Next to Next to Leading Order (NNLO)  $t\bar{t}$  cross section values at the Tevatron and at the LHC is compared in Table 1.3.

Currently the world average top quark mass is measured very precisely by the Tevatron experiments and equals  $173.3 \pm 1.1 \text{ GeV}/c^2$  [12].

	NNLO (pb)
Tevatron ( $\sqrt{s} = 1.96 \text{ TeV}$ )	$7.08^{+0.00+0.36}_{-0.24-0.27}$
LHC ( $\sqrt{s} = 7 \text{ TeV}$ )	$163^{+7+9}_{-5-9}$

**Table 1.3:** The  $t\bar{t}$  cross sections [13] at Tevatron and LHC with  $m_{top} = 173 \text{ GeV}/c^2$  where the first uncertainty is from scale variation between  $m_t/2$  and  $2m_t$  and the second is from MSTW NNLO pdf at 90% CL. The NNLO corrections provide a 7.8% and a 7.6% enhancement over NLO for Tevatron and LHC respectively.

The top quark, which is produced in hadron collisions through strong interactions, decays almost exclusively into a W-boson and a bottom quark. This is shown in Equation (1.6) which calculates the rate of the  $t \rightarrow Wb$  decay by comparing the corresponding branching ratio with the total decay branching ratio. This corresponds to the comparison of the associated CKM matrix components  $V_{tq}$ . Due to the unitarity constraints on the CKM matrix the denominator equals 1 such that the decay rate  $\mathcal{R}$  is totally described by the  $V_{tb}$  component [14].

The decay modes into other down quarks can be neglected and will not be

considered further.

$$\mathcal{R} = \frac{\mathcal{B}(t \rightarrow Wb)}{\mathcal{B}(t \rightarrow Wq)} = \frac{|V_{tb}|^2}{\sum_q |V_{tq}|^2} = |V_{tb}|^2 = 0.998 \quad (1.6)$$

The decay of the top quark is classified according to the decay of the W-boson following either the leptonic or hadronic decay channel. The former has a branching ratio  $\mathcal{B}(W \rightarrow l\nu_l)$  of about  $1/3$  and the latter  $\mathcal{B}(W \rightarrow q\bar{q}) \approx 2/3$ .

The possible  $t\bar{t}$  pairs decay channels and their corresponding branching ratios can be found in Table 1.4. In hadron colliders mainly the all-leptonic or semi-leptonic cases are studied since the all-hadronic decay channel produces six jets which has a large combinatorial ambiguity to group jets into W-boson and top quark objects.

	<b>Decay Channel</b>	<b>Branching Ratio (%)</b>
All-leptonic	$l\nu_l b \ l\nu_l b$	$3 \times 1.2 \quad (l = e, \mu, \tau)$
	$l\nu_l b \ l' \nu_{l'} b$	$3 \times 2.5 \quad (l = e, \mu, \tau)$
Semi-leptonic	$l\nu_l b \ q\bar{q}b$	$3 \times 14.8 \quad (l = e, \mu, \tau)$
All-hadronic	$q\bar{q}b \ q\bar{q}b$	44.4 $(q = u, d, c, s, b)$

**Table 1.4:** The  $t\bar{t}$  decay channels and their branching ratios. The relevant decay channel for this thesis is the semi-leptonic with  $l = \mu$ . The percentages can be given per lepton flavour due to lepton universality, a property not existing for quarks.

The top quark has several remarkable properties, making it the subject of multiple analyses. The unique property that the mass of the top quark is very close to the electroweak breaking scale has large consequences. It raises the question whether the top quark is generated by the Higgs mechanism or if it plays an even more fundamental role in the electroweak breaking mechanism. The high mass also suggests that physics phenomena beyond the Standard Model could have an important interplay with top quark physics, resulting in observed anomalies in top quark production and decays.

More relevant for this thesis is the small lifetime of the top quark, about  $0.5 \times 10^{-24} s$  [1], implying that a top quark decays faster than the characteristic QCD hadronization time. Therefore the top quark is the only quark which can be studied as a free quark. Because of the non-hadronization of the top quark its spin information is transmitted to the decay products, making it possible to measure the W-boson helicity in the top quark decay.

### 1.3 Phenomenology of the Wtb coupling

The decay of a top quark, into a W-boson and a b-quark, is described by the weak Wtb coupling vertex [15, 16]. The most general Wtb vertex can be found in Equation (1.7), with  $q = p_t - p_b$  the four-momentum of the W-boson. At tree level within the Standard Model the form factors  $f_i^{L,R}$  reduce to  $f_1^L = 1$  and  $f_2^L = f_1^R = f_2^R = 0$ .

$$\begin{aligned} \mathcal{L}_{Wtb} = & -\frac{g}{\sqrt{2}} \bar{b} \gamma^\mu V_{tb} (f_1^L P_L + f_1^R P_R) t W_\mu^- \\ & -\frac{g}{\sqrt{2}} \bar{b} \frac{i\sigma^{\mu\nu} q_\nu}{M_W} V_{tb} (f_2^L P_L + f_2^R P_R) t W_\mu^- \end{aligned} \quad (1.7)$$

#### 1.3.1 Weak Charged Current and V-A structure

The observation of maximal parity P violation for the weak interaction in 1956 lead Lee and Yang to propose a V-A (vector - axial vector) structure for the weak force, implying a different action on left- and right-handed fermions. Therefore the charged fermions are split into two parts depending on their chirality or handedness<sup>2</sup>. The left-handed fields are  $SU(2)_L$  doublets while their right-handed partners transform as  $SU(2)_L$  singlets.

The right-handed neutrino does not exist in the Standard Model, as experiments have shown, and thus neutrino's can never acquire mass in the Standard Model.

$$\begin{pmatrix} \nu_l \\ l^- \end{pmatrix}_L ; \begin{pmatrix} q_u \\ q_d \end{pmatrix}_L ; l_R^- ; q_{uR} ; q_{dR} \quad (1.8)$$

In order to well understand the structure of the weak interaction, the difference between helicity and chirality should be clear. The helicity of a particle is defined as the projection of the spin on the direction of flight of the particle. In the used convention a particle is called right-handed when the helicity has a positive value and left-handed when the helicity value is negative, as shown in Figure 1.1. Chirality on the other hand is a more fundamental property and refers to whether the particle transforms in a right- or left-handed representation of the Poincaré group<sup>3</sup>.

These two properties have a subtle difference for massive particles while for massless particles they are equal. This because a massive particle can be observed from a faster traveling reference frame in which the particle appears

<sup>2</sup>Massive particles, such as the charged fermions, with spin  $s$  have  $2s+1$  helicity states while massless particles with spin  $s \neq 0$ , such as the neutral neutrino, always have 2 helicity states. Massless spin-0 particles have only 1 helicity state.

<sup>3</sup>The group of Lorentz transformations, rotations, and translations.

to move backwards, resulting in a reversed helicity value. Since massless particles travel at speed of light there exists no such reference frame, thus helicity and chirality are both frame-independent.



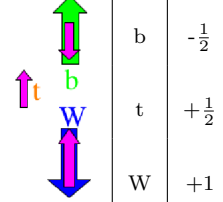
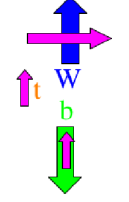
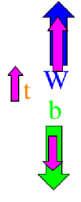
**Figure 1.1:** A right-handed particle has spin and motion in the same direction resulting in a positive helicity value while a left-handed particle has opposite directions and a negative helicity value.

The maximal parity violation in the weak interaction has some important consequences, in particular that massless particles do not appear as right-handed particles. Therefore the charged current interactions, with the  $W^\pm$  bosons, only couple with left-handed fermions and right-handed antifermions.

For the  $Wtb$  coupling this V-A structure implies an entirely left-handed interaction such that the top quark decays as a left-handed fermion. Specific for the  $Wtb$  coupling is that the b-quark is assumed to be massless, in comparison with the W-boson and the top quark, such that only the left-handed b-quark is allowed. This explains the suppression of the right-handed W-boson as it should be accompanied with the left-handed b-quark. Such a combination is forbidden by angular momentum. Hence the right-handed W-boson only appears in the  $Wtb$  interaction when combined with a right-handed b-quark. Since the b-quark is not completely massless right-handed b-quarks can occur in the  $Wtb$  interaction, although heavily restricted. This is indeed shown in Table 1.5, with only a very small fraction for the positive helicity or right-handed W-boson configuration.

The obtained polarization state of the W-boson influences the angular distribution of its decay products. This dependence can be parametrized by introducing the angle  $\theta^*$ , which is defined as the angle between the down-type fermion from the W-boson decay in the W-boson rest frame and the W-boson in the top quark rest frame.

From the conservation of angular momentum, shown in Figures 1.2(a) - 1.2(c), follows that  $\theta^*$  has most of its probability density between  $135^\circ - 225^\circ$ ,  $-45^\circ - 45^\circ$  and  $45^\circ - 135^\circ$  for the left-handed, right-handed and long-

Negative helicity			Zero helicity			Positive helicity					
	Spin		Fraction		Spin		Fraction		Spin		Fraction
	b	$-\frac{1}{2}$	0.30		W	0	0.70		W	+1	$3.6 \times 10^{-4}$
	t	$+\frac{1}{2}$			t	$+\frac{1}{2}$			t	$+\frac{1}{2}$	
	W	+1			b	$+\frac{1}{2}$			b	$-\frac{1}{2}$	

**Table 1.5:** Possible configurations for the W-boson helicity with their corresponding relative fractions. These fractions represent the Standard Model helicity values [17]. The narrow pink arrows indicate the spin vectors while the others indicate the particle's momentum.

itudinal polarization respectively. This can be retrieved in Figure 1.2(d), showing the corresponding angular  $\cos \theta^*$  distribution for the different polarizations. The solid black line represents the total Standard Model angular distribution which should be obtained in experimental observations.

### 1.3.2 The CKM matrix

As demonstrated in Equation (1.7), the  $Wtb$  interaction includes the  $V_{tb}$  component of the Cabibbo-Kobayashi-Maskawa (CKM) matrix, which is an extension of the Glashow-Iliopoulos-Maiani GIM mechanism [18]. It states that the weak interaction states are superpositions of the mass eigenstates. The corresponding transformation matrix is, in the case of only two quark families, a simple rotation matrix with only one real parameter. In 1973 M. Kobayashi and T. Maskawa postulated the existence of a third quark family in order to account for the observed CP violation in weak kaon decays. A third generation implies that the transformation matrix has three real parameters and one complex phase, necessary for CP violation.

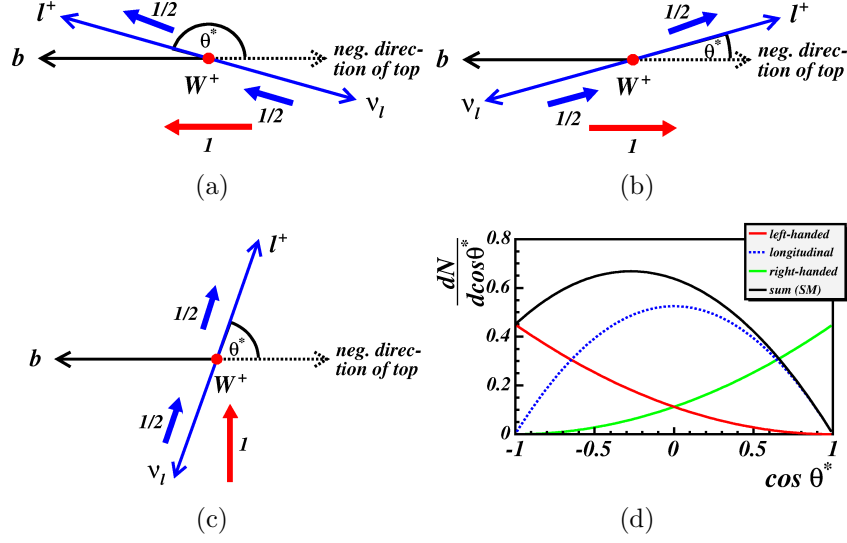


**Figure 1.2:** a)-c) Angular distribution for left-handed, right-handed and longitudinal W-boson polarization. d) Theoretical angular distribution for left-handed (red), right-handed (green) and longitudinal (blue dashed) W-boson polarization. The solid black line indicates the overall angular distribution.

Equations (1.9) show the different representations of the CKM matrix, the form used in Equation (1.9b) is called the Wolfenstein parametrization [19] which exhibits the hierarchy of the matrix. Relevant for the Wtb interaction is the  $V_{tb}$  component of the CKM matrix.

The magnitudes [14] of all nine CKM elements given in Equation (1.9c) are obtained by applying a global fit on all available measurements, combined with the Standard Model constraints (i.e. three generations, unitarity).

$$V = \begin{pmatrix} V_{ud} & V_{us} & V_{ub} \\ V_{cd} & V_{cs} & V_{cb} \\ V_{td} & V_{ts} & V_{tb} \end{pmatrix} \quad (1.9a)$$

$$= \begin{pmatrix} 1 - \lambda^2/2 & \lambda & A\lambda^3(\rho - i\eta) \\ -\lambda & 1 - \lambda^2/2 & A\lambda^2 \\ A\lambda^3(1 - \rho - i\eta) & -A\lambda^2 & 1 \end{pmatrix} \quad (1.9b)$$

$$= \begin{pmatrix} 0.97428 \pm 0.00015 & 0.2253 \pm 0.0007 & 0.00347^{+0.00016}_{-0.00012} \\ 0.2252 \pm 0.0007 & 0.97345^{+0.00015}_{-0.00016} & 0.0410^{+0.0011}_{-0.0007} \\ 0.00862^{+0.00026}_{-0.00020} & 0.0403^{+0.0011}_{-0.0007} & 0.999152^{+0.000030}_{-0.000045} \end{pmatrix} \quad (1.9c)$$

### 1.3.3 Measuring W helicities

In this thesis the Standard Model constraints will be used for the  $Wtb$  interaction, implying that Equation (1.7) reduces to (1.10).

$$\mathcal{L}_{Wtb} = -\frac{g}{\sqrt{2}}\bar{b}\gamma^\mu V_{tb}P_L t W_\mu^- \quad (1.10)$$

In order to measure the helicity of the W-boson in top quark decays the angular distribution between the down-type fermion in the W-boson decay and the W-boson itself will be studied in detail. In this thesis one W-boson decays leptonically into a muon and a muon-neutrino and the other W-boson decays hadronically, thus a semi-muonic  $t\bar{t}$  decay is considered.

The observation of a significant deviation from the angular distribution shown in Figure 1.2(d) would be an unambiguous indication of new physics.

# Chapter 2

## The CMS Experiment at the LHC

### 2.1 The Large Hadron Collider

The Large Hadron Collider (LHC) [20, 21] is located at CERN (the European Organization for Nuclear Research), near Geneva. It is built in the former circular LEP (Large Electron-Positron Collider) tunnel, which has a circumference of about 27 km.

The Large Hadron Collider was designed to yield head-on collisions of two proton (ion) beams of 7 TeV (2.75 TeV per nucleon) each, with a design instantaneous luminosity of  $10^{34} \text{cm}^{-2} \text{s}^{-1}$ . The accelerator is operational since autumn 2009 and currently, since March 2010, protons are colliding at a centre-of-mass energy of 7 TeV.

Even with this current energy the LHC is the world's most energetic particle collider, before Fermilab's Tevatron  $p\bar{p}$  collider with a centre-of-mass energy of 1.96 TeV.

The LHC will accelerate proton beams with an initial energy of 450 GeV such that smaller pre-accelerators are needed, shown in Figure 2.1 which represents the complete CERN accelerator complex. First protons are accelerated by the linear LINAC2 pre-accelerator. In a next step the 50 MeV protons are injected into the Proton Synchrotron Booster (PSB) and accelerated up to 1.4 GeV. The larger Proton Synchrotron (PS) will further increase the energy to 26 GeV such that the proton beams can be injected into the last pre-accelerator, the Super Proton Synchrotron (SPS). Here the protons will be accelerated to 450 GeV.

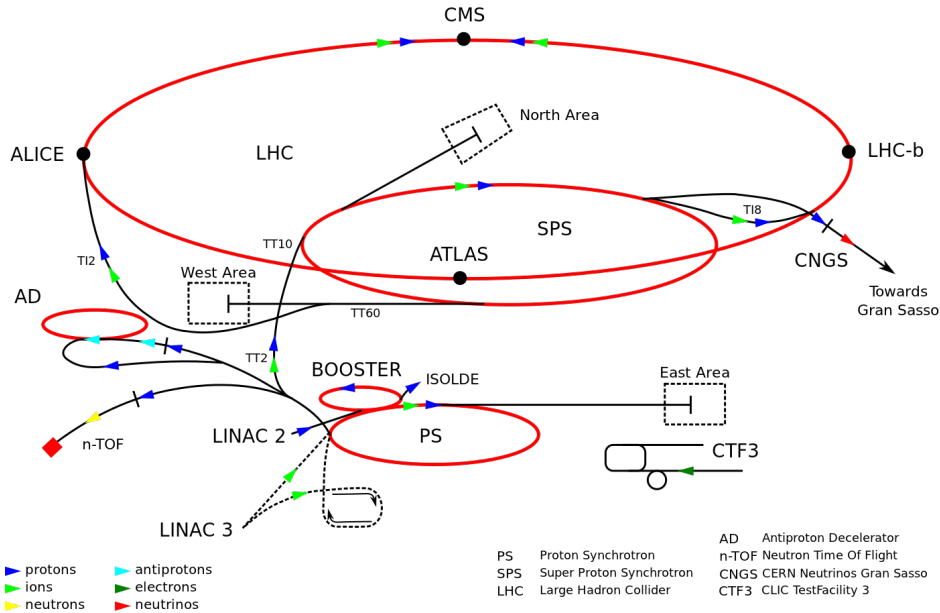


**Figure 2.1:** The CERN accelerator complex.

The Large Hadron Collider circulates the same particles, namely protons or ions, in different directions. This is contrary to the Tevatron which is a proton-antiproton collider. This implies that two separate beam pipes are needed with magnetic field in opposite directions. Hence the LHC consists of 1 232 superconducting dipoles and 2 500 other magnets. These dipoles, for which an overview is given in Figure 2.2, will operate at a temperature of 1.9 K and will produce a magnetic field of 8.33 T for proton beams circulating with an energy of 7 TeV. Since currently the total centre-of-mass energy is only 3.5 TeV, the produced magnetic field is only 4.15 T.

For the designed 14 TeV the LHC expected to circulate 2 808 bunches of about  $10^{11}$  protons, with only 25 ns bunch spacing. This would result in a luminosity of  $10^{34} \text{ cm}^{-2} \text{ s}^{-1}$ .

Currently only about half of the energy is reached such that the maximal obtained luminosity for 2010 data was about  $2 \times 10^{32} \text{ cm}^{-2} \text{ s}^{-1}$ . The acquired number of bunches was 368 with a bunch spacing of 150 ns.

Even the current bunch spacing is more than 2 times higher than the one used in Tevatron. Such a low bunch spacing has as consequence that the detector signals are not all processed when the following collision enters. Hence this will result into out-of-time pile-up which implies that the previous collision pollutes the analyzed event. For hadron colliders also in-time pile-up occurs when multiple collisions take place during one event.

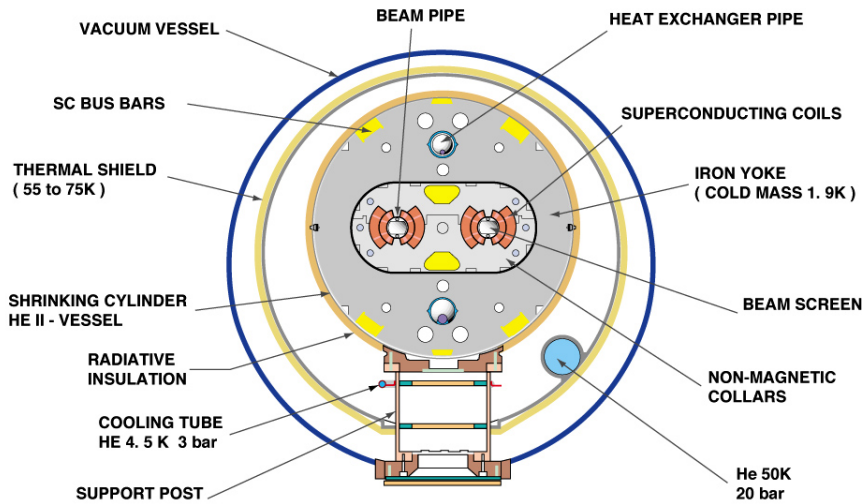


Figure 2.2: Cross-sectional view of a LHC dipole magnet.

### 2.1.1 Experiments at the LHC

Experiments built around the Large Hadron Collider complex need account for the major difficulties originating from such a high-energetic proton accelerator. Due to the huge event rate, approximately  $10^9$  inelastic events/s, an efficient event selection trigger is needed since only about 300 events/s, 300Hz, can be stored and further analyzed.

Also the short time between the different bunch crossings indicates the need of high-granularity detectors with good time resolution to reduce the pile-up effects. Hence a good momentum resolution and reconstruction efficiency is needed in all detectors.

The experiments fulfilling these requirements are the two general-purpose detectors, namely the Compact Muon Solenoid (CMS) [22, 23] and A Toroidal LHC ApparatuS (ATLAS) [24]. As the names suggest, the main difference between these two detectors is the used magnet. CMS uses a powerful solenoid field while ATLAS uses an external toroid field combined with a smaller inner solenoid.

The other four experiments, ALICE [25], LHC-b [26], TOTEM [27] and LHC-f [28], are constructed to study specific signals and thus have different requirements. The ALICE (A Large Ion Collider Experiment) detector will look in detail to the heavy ion collisions and study the quark-gluon plasma. The LHC-b (Large Hadron Collider beauty) is specialized in b-flavour physics and will look for the origin of CP-violation in the B-system. The two remaining

smaller detectors, TOTEM and LHC-f, are located in the interaction points of respectively CMS and ATLAS and will study physics in the forward region of the proton-proton collisions.

## 2.2 The Compact Muon Solenoid

The Compact Muon Solenoid, one of the two general-purpose detectors at the LHC, consists of four different detector subsystems and is characterized by a superconducting solenoid accommodating an inner tracker and calorimetry inside. The detector has a length of 21.3m, a diameter of 14.6m and a total weight of 12 500 tons.

The CMS detector has a very good muon system and solenoidal field of 3.8 T. Inside this powerful solenoid the state-of-the-art Electromagnetic calorimeter is located which is optimized for the Higgs boson decay signal of two photons. The complete calorimetry, electromagnetic and hadronic calorimeter combined, is hermetically closed in order to reconstruct non-interacting high-energetic particles, such as the neutrino. Inside the calorimetry the full-silicon-based inner tracking system can be found, responsible for precise vertex reconstruction of charged particles.

An overview of the different CMS detector subsystems is given in Figure 2.3.

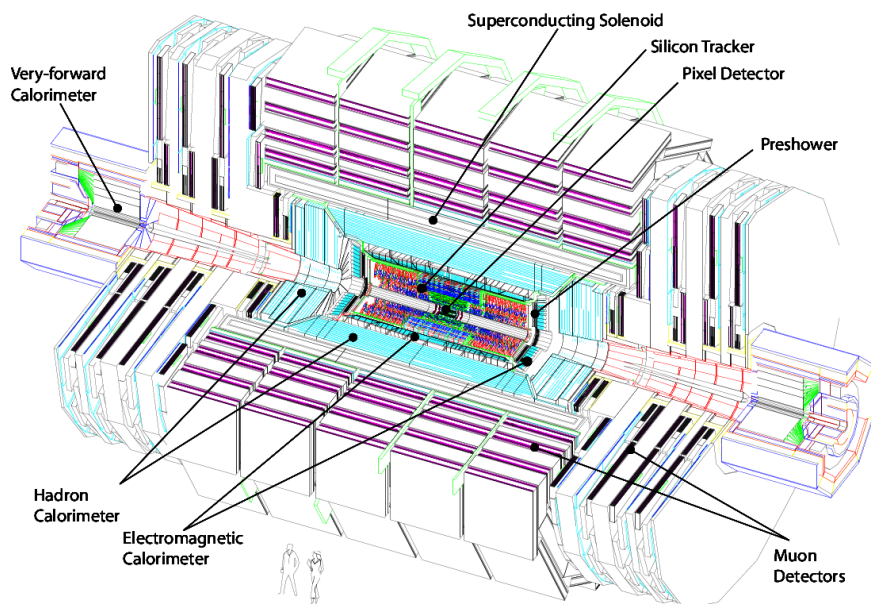


**Figure 2.3:** Schematic layout of the Compact Muon Solenoid experiment [29].

From Figure 2.3 the detector configuration with central barrel and outer endcap regions is clearly visible. The same structure can also be found in the different subsystems which will be discussed in detail. The return yoke for the magnetic field placed between the muon detectors is also shown in this figure. It ensures an additional bending of the muon path, represented in Figure 2.4, such that an accurate  $p_T$  measurement is possible. Figure 2.4 also describes the path and detector signal of the different particles in the subsystems of the CMS detector. The influence of the strong magnetic solenoid is clearly visible.

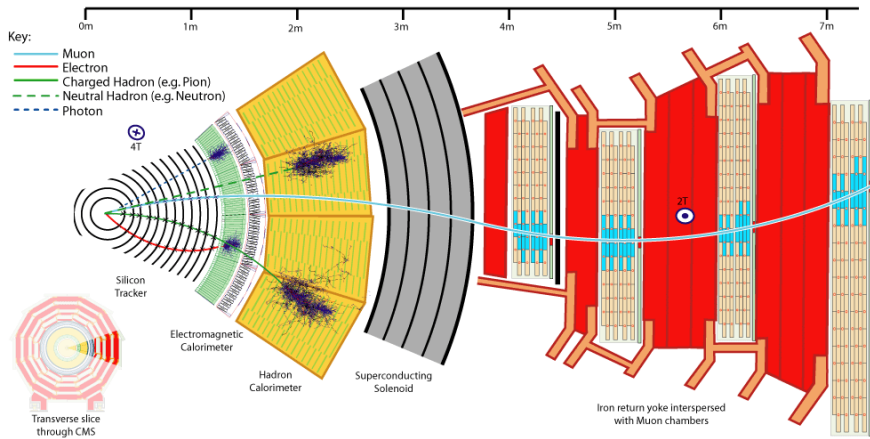


**Figure 2.4:** Flight path of the different particles in the subdetectors of the CMS experiment.

The CMS detector has a specific coordinate system for which the origin is located at the nominal collision point inside the experiment. This coordinate system will be used further in this thesis.

The  $x$ -axis is pointing radially inward towards the center of the LHC ring and the  $y$ -axis is pointing vertically upward. The  $z$ -axis is pointing along the beam direction towards the Jura mountains, as seen from LHC Point-5 of the CMS detector. The azimuthal angle  $\phi$  is measured from the  $x$ -axis in the  $x$ - $y$  plane and the polar angle  $\theta$  is measured from the  $z$ -axis. The Lorentz invariant pseudorapidity, defined as  $\eta = -\ln \tan(\theta/2)$ , is an important quantity in experimental physics. It will be shown in the schematic overview of all CMS subdetectors to represent the covered range.

### 2.2.1 The Silicon Tracker

The CMS tracking detector is the most inner detector of the four subsystems and is located around the interaction point. The inner tracking system has a length of 5.8m and a diameter of 2.5m and is the largest silicon tracker ever build. It is designed to reconstruct the tracks of all the charged particles emerging from the collisions and has a total pseudorapidity acceptance of  $|\eta| < 2.5$ .

The CMS tracker consists of a multi-layered silicon microstrip detector and a multi-layered silicon pixel detector. The former one provides granularity and precision and the latter improves the measurement of the impact parameter of charged-particle tracks as well as the position of secondary vertices. The pixel detector is positioned closest to the interaction point with the surrounding silicon strip detector.

The silicon tracker configuration is given in Figure 2.5, which also shows the three barrel layers of the microstrip tracker (TID, TOB and TIB) and the two endcap disks (TEC+ and TEC-).

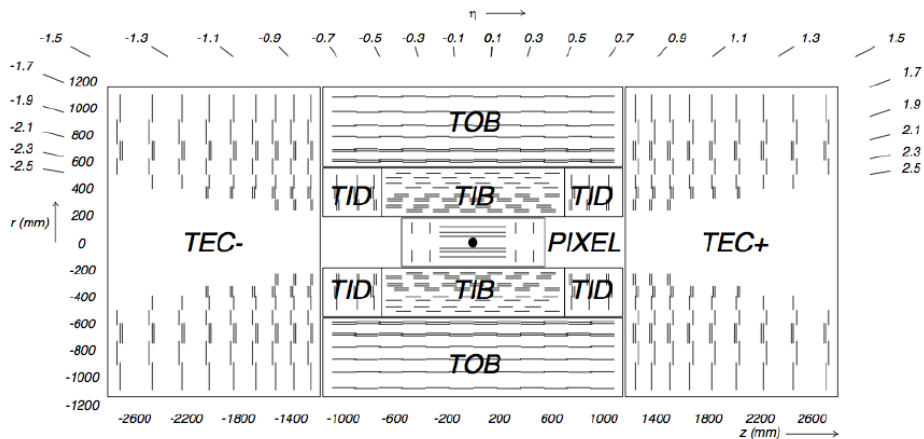


**Figure 2.5:** Schematic overview of the CMS silicon tracker system.

### 2.2.2 The Electromagnetic Calorimeter

The Electromagnetic Calorimeter (ECAL) is a homogeneous calorimeter made of lead tungstate ( $\text{PbWO}_4$ ) crystals since these high density crystals result in a fast, high granular and radiation resistant calorimeter. Hence all the characteristics needed in the LHC environment.

The ECAL provides a full pseudorapidity coverage of  $|\eta| < 3.0$  and is designed

to precisely measure the decay of the Higgs boson  $H$  into two photons. The Electromagnetic Calorimeter is of crucial importance for the identification of electrons and photons and for a precise measurement of their energy and direction.

Figure 2.6 shows the geometry of the Electromagnetic Calorimeter which again has a barrel and endcap structure. The endcap region has an extra preshower detector (ES), with the principal aim to identify neutral pions in the endcaps such that the signals  $H \rightarrow \gamma\gamma$  and  $\pi^0 \rightarrow \gamma\gamma$  can be distinguished.

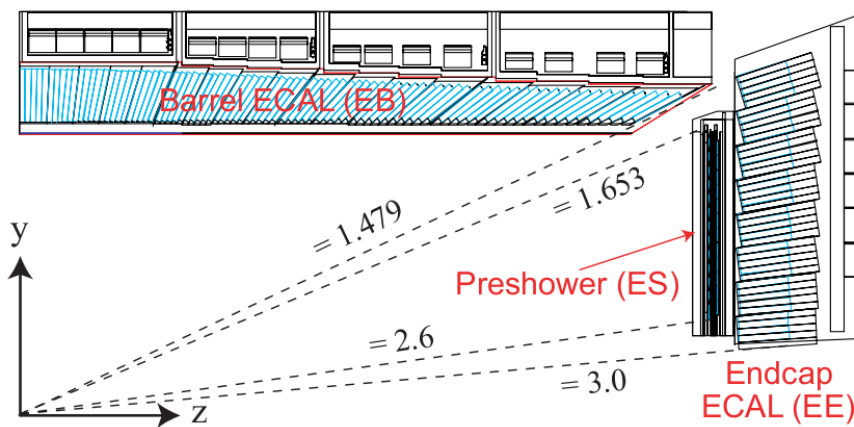


Figure 2.6: Layout of the Electromagnetic Calorimeter.

### 2.2.3 The Hadronic Calorimeter

Around the ECAL the Hadronic Calorimeter (HCAL) is placed which is designed to measure the energy of hadrons. Since it was decided to place both the electromagnetic as the hadronic calorimeter inside the solenoid, the amount of material used to absorb the hadronic shower was heavily restricted. Therefore an outer hadron calorimeter (Hadron Outer) was placed outside the solenoid complementing the barrel calorimeter.

Figure 2.7 represents the layout of the Hadronic Calorimeter and indicates that it consists of four different sub-calorimeters, namely the HO outside the solenoid and the Hadron Barrel (HB), Hadron Endcap (HE) and Hadron Forward (HF).

The HB and HE are sampling calorimeters with brass (70%Cu, 30%Zn) as absorber which have a pseudorapidity range of respectively  $|\eta| < 1.3$  and  $1.3 < |\eta| < 3$ . The extra hadron calorimeter placed outside the solenoid is needed in the central region of  $|\eta| < 1.3$  in order to sufficiently contain the

hadron showers leaking through the rear of the central calorimeters. The Hadron Forward (HF) extends the total coverage from  $|\eta| = 3$  up to  $|\eta| = 5.2$ . Since it will experience unprecedented particle fluxes it consists of steel absorbers and quartz fibers emitting Cherenkov light.

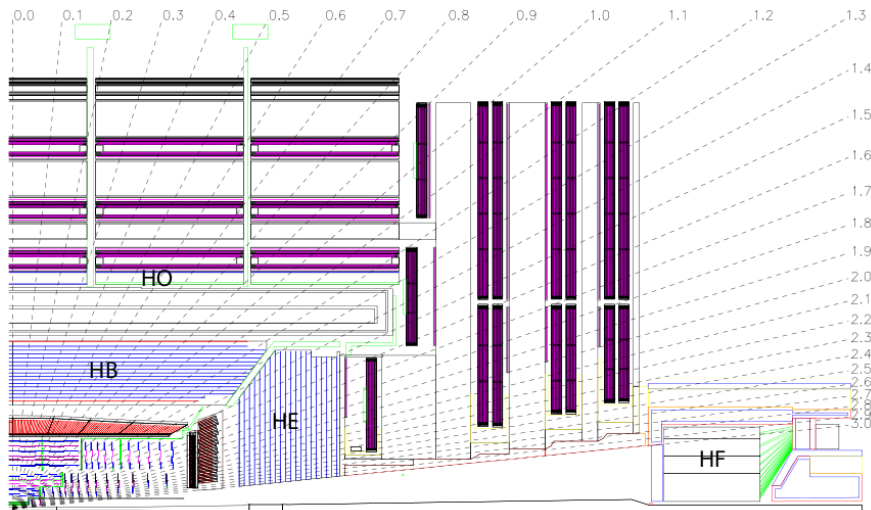


**Figure 2.7:** Overview of the different HCAL calorimeters.

## 2.2.4 The Muon System

As the middle name of the Compact Muon Solenoid experiment suggest, muon identification is essential for recognizing signatures of interest over the enormous background. Since muons go through the entire detector while depositing only a minimum of energy, the large CMS Muon System is placed outside the solenoid. The muon detectors are interleaved with iron yokes to provide stopping power and uses three types of gaseous particle detectors. The Muon System is shown in Figure 2.8, again with a clear barrel and end-cap structure.

In the barrel region, where the muon rate is low, Drift Tubes (DT) are used with a pseudorapidity coverage of  $|\eta| < 1.2$ . The endcaps region uses Cathode Strip Chambers (CSC) to account for the higher muon rate. This endcap region extends the total coverage to  $|\eta| < 2.4$  and has an overlap with the barrel region for  $|\eta|$  values between 0.9 and 1.2. The main part of the Muon System,  $|\eta| < 1.6$ , is complemented with Resistive Plate Chambers (RPC) which are used for trigger purposes due to the fast response and good time resolution.

The Muon System will be combined with the inner tracker detector to reconstruct the complete muon tracks through the whole CMS detector.

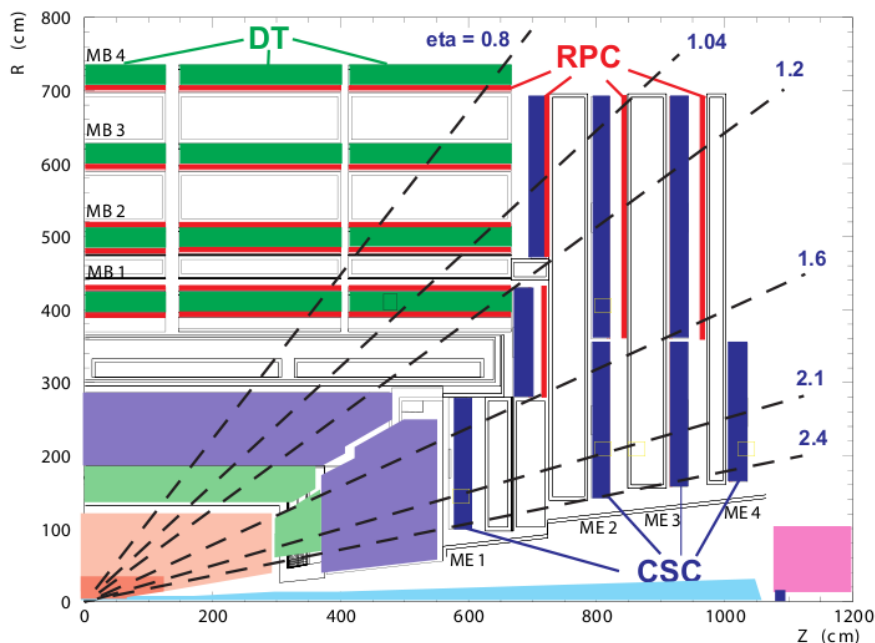


**Figure 2.8:** Schematic view of the CMS Muon System.

## 2.2.5 The Trigger System

The CMS Trigger System reduces the data event rate of 40 MHz down to about 10 Hz, the maximum rate which can be stored and used for offline analysis. It consists of two triggers, namely the Level-1 (L1) Trigger which has only  $3.2\mu\text{s}$  to decide to keep an event for further analysis and store the event information in so-called pipelines and the High-Level Trigger (HLT). The L1 Trigger consists of custom-designed electronics which only has access to the calorimeter and muon system information. In order to ensure such a fast triggering the electronics are located partly on the detector and partly in the underground control room at approximately 90 m of the CMS detector. After the L1 Trigger the event rate has been reduced to 300 kHz. The HLT is a more complex software system implemented in a filter farm of about one thousand commercial processors, located at the surface. In contrary to the L1 Trigger the HLT has access to the complete read-out data such that it assimilates and synchronizes information from different parts of the detector to recreate the entire event and keep the events of interest.

## 2.3 Simulating proton collisions

For the analysis made in this thesis simulated events will be used to compare against the collected data events. In the CMS experiment these simulated events are produced with the CMS SoftWare framework (CMSSW). This framework will ensure the event generation, the simulation of the full CMS detector and the reconstruction of the particles present in the events.

The production of simulated events is consists of different steps, which are all performed by specific programs. The first step, the generation of the events, is done with Monte-Carlo generators MadGraph [30] and PYTHIA [31]. In general MadGraph will generate the parton-level of the proton-proton collision while PYTHIA will perform the fragmentation and hadronization. Only for the muon-enriched<sup>1</sup> QCD sample the entire event generation is done by PYTHIA.

In the next step the generated particles are sent through a full CMS detector simulation, using the GEANT4 software [32]. Here the interactions of the particles as they cross the CMS detector are simulated. Also the measured hits of the simulated events will be digitized by simulating the electronics response. Hence the simulation will comprise the same detector effects as data, namely interaction with cables, badly working electronics, etc..

Since such a full simulation is very CPU intensive and thus time-consuming a simplified simulation, called FastSim. This simulation will not be used in this thesis.

The different used simulation samples together with their cross section and integrated luminosity can be found in Table 2.1.

## 2.4 Data taking in 2010

The Large Hadron Collider started colliding protons on 30 March 2010 with a beam energy of 3.5 TeV. Since the CMS detector is shut down from time to time, not all of the delivered luminosity will be recorded. From the delivered integrated luminosity of 46.41 pb<sup>-1</sup> by the LHC, the CMS experiment has only recorded 43.11 pb<sup>-1</sup>. Hence an efficiency of 92.89 %. Finally for analysis purposes, the amount of certified integrated luminosity is important. This is the amount of recorded luminosity for which no problems with the detector were observed. For the 2010 data taking a certified luminosity of 36.13 pb<sup>-1</sup>

---

<sup>1</sup>Only QCD events which have on parton level a muon with  $p_T$  higher than 15 GeV/c are kept for further analysis.

	<b>Luminosity (pb<sup>-1</sup>)</b>	<b>Cross section (pb)</b>
<i>t<math>\bar{t}</math> semi-<math>\mu</math></i>	7 805.2	23.33
<i>t<math>\bar{t}</math> other</i>	7 823.8	134.17
<b>single t (tW Channel)</b>	46 694.4	10.6
<b>single t (t Channel)</b>	23 127.6	20.93
<b>Z + jets</b>	632.24	3 048
<b>W + jets</b>	352.84	31 314
<b>QCD</b>	163.18	84 679.3

**Table 2.1:** Used simulation samples with collected luminosity and theoretical cross section.

is obtained, hence an efficiency of 83.81 %.

The above numbers have been summarized in Figure 2.10.

The 2010 run was executed with an average instantaneous luminosity of  $2 \times 10^{32} \text{ cm}^{-2} \text{ s}^{-1}$  and an integrated luminosity of  $36.13 \text{ pb}^{-1}$ . During the 2010 run the bunches were separated with a bunch spacing of 150 ns. Hence the influence of out-of-time pile-up was negligible. This will definitely change in the 2011 run where the bunch spacing has been lowered to 50 ns. The in-time pile-up did occur with an average of about 2.67 pile-up events per bunch crossing in CMS [33]. The distribution for the in-time pile-up is given in Figure 2.9.

With the  $t\bar{t}$  cross section given in Table 1.3 and the amount of certified luminosity known, the number of  $t\bar{t}$  events measured in the 2010 run can be calculated. Hence about 5 884  $t\bar{t}$  events are expected in the data sample. Since semi-muonic  $t\bar{t}$  events only appear in 4/27 of the cases about 870 of these event should take place. With the 2011 run, currently already about  $780 \text{ pb}^{-1}$  has been recorded, this number is increased to 18 836 semi-muonic  $t\bar{t}$  events.

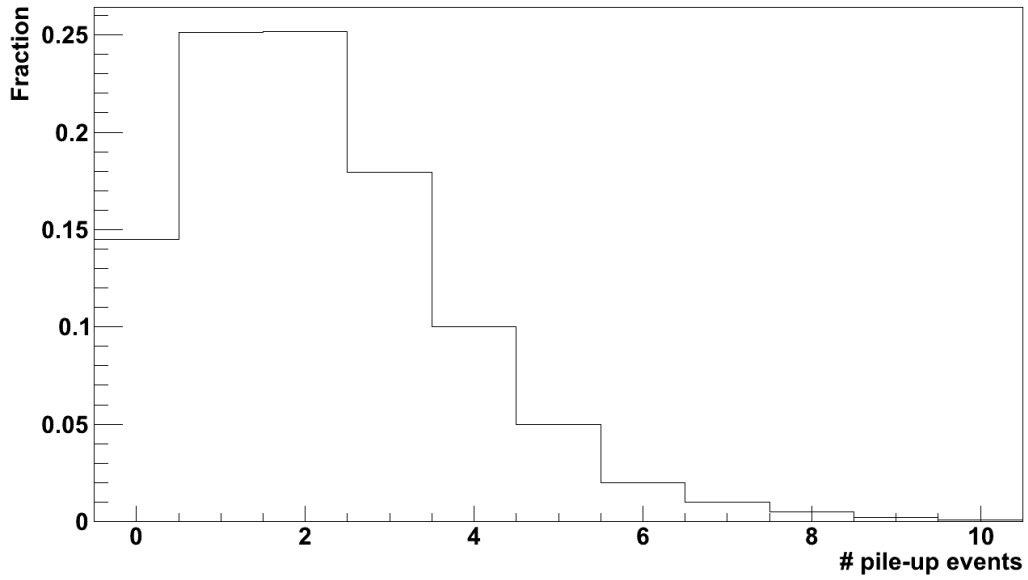


Figure 2.9: Fraction of in-time pile-up events.

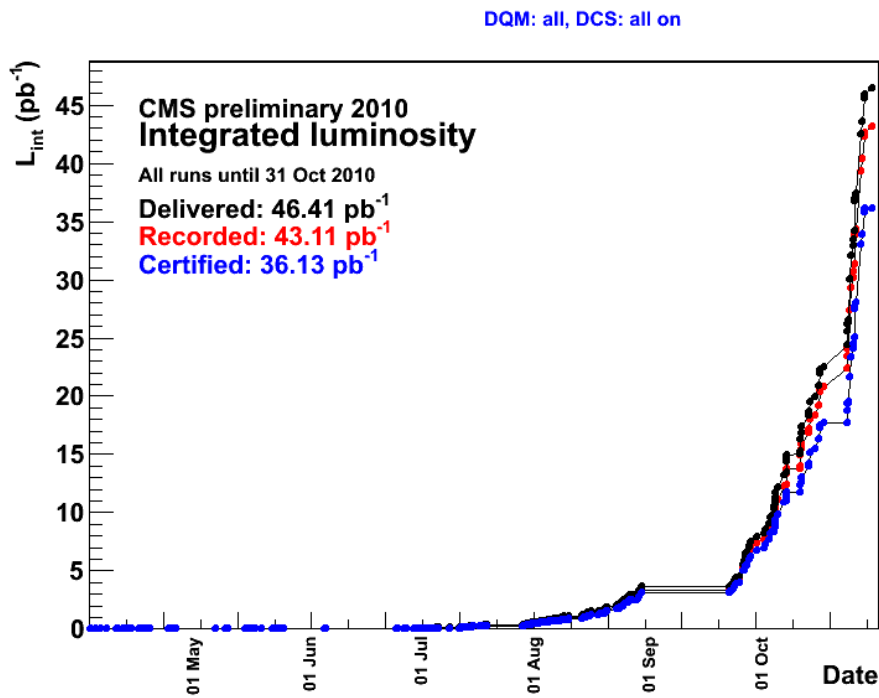


Figure 2.10: Integrated luminosity in CMS.

# Chapter 3

## Reconstruction of top-pair events

In the previous chapter the different subdetectors and the data-handling were covered. This chapter will focus on the reconstruction of the physics event combining the detected data in the different subsystems. A correct representation of the final state particles is of crucial importance in each analysis. Since this thesis only considers semi-muonic decaying  $t\bar{t}$  events,  $t\bar{t} \rightarrow bW\bar{W}b \rightarrow bj\bar{j}\mu\bar{\nu}_\mu\bar{b}$ , the relevant reconstruction tools involve muons, jets, missing energy and b-flavour identification.

### 3.1 Jet Reconstruction

Every event in hadron collisions is characterized by the presence of final state quarks. Reconstructing these quarks is a major challenge since, due to QCD confinement, color charged particles do not exist and thus fragment into color neutral bound states. This hadronization process produces a narrow flow of hadrons, defined as a jet, of which the properties will be used to reconstruct the momentum and energy of the original parton.

In the CMS detector this is done by the ParticleFlow method [34], which identifies all charged particles in the event by combining data from the central silicon tracker and both calorimeters. Tracks reconstructed in the silicon tracker are extrapolated to the electromagnetic and hadronic calorimeter. They are linked to a calorimeter cluster if the extrapolation of the track falls within the boundaries of one of the energy deposits in the cluster.

Neutral particles are reconstructed from calorimetric energy clusters only. The expected energy deposits of the charged particles is calculated by the sum of the associated track momenta. Remaining calorimeter clusters are

considered as neutral particles. Hence neutral particles are most accurately reconstructed when the clusters are separated from the extrapolated position of tracks.

The main advantage of this method is that the particle's momentum is obtained at the vertex, before its direction and momentum is influenced by the strong magnetic field of the superconducting solenoid.

The jets are reconstructed with the anti- $k_T$  jet algorithm [35], for which the input objects are obtained from the ParticleFlow method.

A jet reconstruction algorithm introduces distances  $d_{ij}$  between entities  $i$  and  $j$  and  $d_{iB}$  between entity  $i$  and the beam, as defined in Equation (3.1). The clustering then proceeds by identifying the smallest of all the distances. If this smallest distance is between two entities, they will be combined into one entity. If it is between an entity and the beam, the corresponding entity will be called a jet and will be removed from the list of entities. This method is repeated until no entities remain.

Equation (3.1) shows the used definition of the distance measures where  $\Delta_{ij}^2 = (y_i - y_j)^2 + (\phi_i - \phi_j)^2$  and  $k_{ti}$ ,  $y_i$  and  $\phi_i$  are respectively the transverse momentum, rapidity and azimuth of particle  $i$ . The distance parameter  $R$  used for the width of the jet is set to 0.5.

$$d_{ij} = \min(1/k_{ti}^2, 1/k_{tj}^2) \frac{\Delta_{ij}^2}{R^2} \quad (3.1a)$$

$$d_{iB} = k_{ti}^{-2} \quad (3.1b)$$

This algorithm has the feature that soft particles do not modify the shape of the jet, in contrary to hard particles.

When two particles are combined during the algorithm their four-momenta are combined according to a recombination scheme. This describes how the constituents of the jet are added together to calculate the properties of the jet. The used scheme in this thesis is the Energy or E-scheme for which the constituents are simply added as four-vectors. The resulting four-vector then represent the kinematic properties of the jet.

The momenta of the reconstructed jets correspond to the raw measured energy deposits. Numerous influences could substantially change the obtained jet energy from the original parton energy, for which corrections should be applied. In the CMS collaboration it was chosen to use a factorized multi-level jet energy calibration method consisting of a correction factor for each detector system and physics effect. The fixed order in which these different correction levels should be applied is listed below.

- **Offset correction (Level-1)**  
Corrects for the effect of electronic noise and pile-up of multiple proton collisions, resulting in a luminosity independent sample.
- **Relative  $\eta$  dependent correction (Level-2)**  
Flattens the jet response dependency on the pseudo-rapidity to account for the pseudo-rapidity transition regions between different calorimeter subsystems with a too low jet energy response.
- **Absolute  $p_T$  dependent correction (Level-3)**  
This correction makes the jet response in function of the jet  $p_T$  flat.
- **Correction for dependency on electromagnetic fraction (Level-4)**  
Improves the jet energy resolution by taking into account the deposited electromagnetic energy fraction.
- **Correction for dependency on the jet flavour (Level-5)**  
The flavour of the parton from which the jet originates influences the momentum of the fragmented particles and the possible presence of neutrinos, which lowers the jet response.
- **Correction for the underlying event (Level-6)**  
Corrects for the contribution of underlying event energy to the jet energy.
- **Correction to the parton level (Level-7)**  
Corrects back to the parton level such that the corrected jet  $p_T$  is equal to the originating parton on average.

The above explained jet energy corrections were obtained with simulated events. After collecting and analyzing the first available 7 TeV collision data it was realized that the comparison between simulation and data indicates small deviations. Therefore a residual calibration was developed to correct for these small differences, which should only be applied to data-samples. In this thesis the simulated samples will be corrected with Level-2 and Level-3 jet energy calibrations and the used data sample with Level-1, Level-2 and Level-3 calibrations.

Figure 3.1 represents the properties of the jets present in semi-muonic  $t\bar{t}$  events. Figure 3.1(a) indicates that a large number of jets are measured in semi-muonic  $t\bar{t}$  events. When the jets are required to have transverse momentum higher than 30 GeV/c, a value which will be used in Chapter 4,

the number of jets in one event is significantly lowered. Figure 3.1(b) shows that the leading jet<sup>1</sup> in such events has a  $p_T$  of about 100 GeV/c such that the  $p_T > 30$  GeV/c requirement can be justified. Figure 3.1(c) indicates that the many low  $p_T$  jets present in semi-muonic  $t\bar{t}$  events have little contribution to the scalar sum of the transverse momenta all jets. The obtained distribution is only shifted with about 100 GeV/c after the exclusions of jets with  $p_T < 30$  GeV/c. The peak present for  $H_T = 1200$  GeV/c has no physical meaning but represents the overflow bin. This contains all the entries which fall outside the considered range. Figure 3.1(d) finally shows that the leading jet can be found in the pseudorapidity region  $|\eta| < 3$ , the region which is fully covered by the electromagnetic and hadronic calorimeter.

These figures, and all the following figures in this chapter, are obtained from simulations for semi-muonic  $t\bar{t}$  events.

## 3.2 Muon Reconstruction

The presence of a muon in semi-muonic  $t\bar{t}$  events is of crucial importance to distinguish these events from the QCD multi-jet background collected with the CMS detector. In order to correctly reconstruct the muon, the CMS detector combines information from the silicon tracker at the heart of the detector and the muon system installed outside the solenoid.

In the standard CMS reconstruction of pp collisions, three different muon reconstruction approaches exist [36]. This because the independently reconstructed tracks in the silicon detector (*tracker track*) and in the muon system (*standalone-muon track*) can be combined in different ways.

The standalone muon reconstruction only uses information from the muon system, namely the drift tubes, cathode strip chambers and resistive plate chambers. A Kalman filter [37] starts from the seeds, identified in the innermost chambers by local reconstruction, and builds the trajectories through each layer in an inside-out way. When the outermost layer is reached, an additional outside-in Kalman filter provides the track parameters, extrapolation to the interaction point and a vertex constraint.

The Global Muon reconstruction is an outside-in method which starts from a standalone muon and determines a region of interest in the silicon layers compatible with the muon track. In this region of interest, seeds are built

---

<sup>1</sup>A leading particle is the particle from the entire collection with the highest transverse momentum. The transverse momentum  $p_T$  is defined as  $\sqrt{p_x^2 + p_y^2}$ .

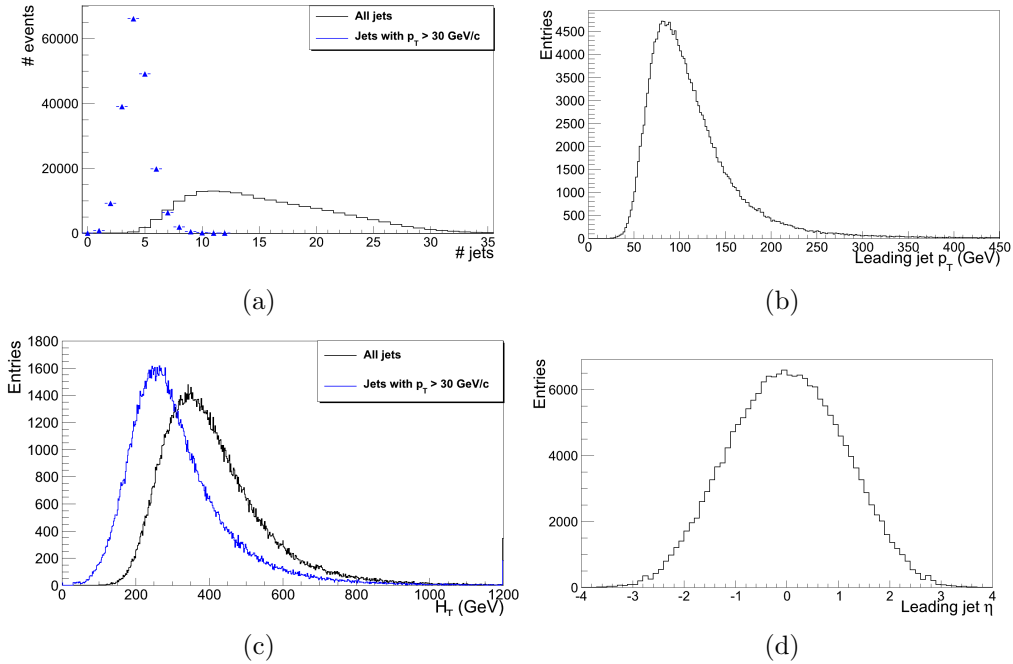


**Figure 3.1:** a) Number of jets (black curve) and number of jets with transverse momentum higher than 30 GeV/c (blue triangles) in semi-muonic  $t\bar{t}$  events. b) Transverse momentum of the leading jet. c) Scalar sum of the transverse momenta of all jets (black) and all jets with  $p_T$  higher than 30 GeV/c (blue). d) Pseudorapidity of the leading jet.

from pairs of reconstructed hits. Again a Kalman filter constructs the track from these seeds inside the region of interest. In a final step a global refit of the track is done, using the obtained hits from the muon system and the silicon tracker.

The Tracker Muon reconstruction starts from tracks in the silicon detector and looks for compatible signatures in the calorimeters and the muon system. This algorithm is particularly useful for the identification of low momentum muons.

Figure 3.2(a) shows the number of muons present in a semi-muonic  $t\bar{t}$  event compared with the number present when a  $p_T$  larger than 20 GeV/c is required. Such a constraint gives a significant peak of 1 muon in the event, which is expected in semi-muonic  $t\bar{t}$  events. Figures 3.2(b) and 3.2(c) give the distribution for the transverse momentum and pseudo-rapidity  $\eta$  of the leading muon. The momentum distribution peaks at 30 GeV/c, while the pseudorapidity is restricted by the  $|\eta| < 2.4$  acceptance region of the muon

system. Figure 3.2(d) gives the number of hits in the inner tracker for a muon path. An average of about 17 hits is obtained.

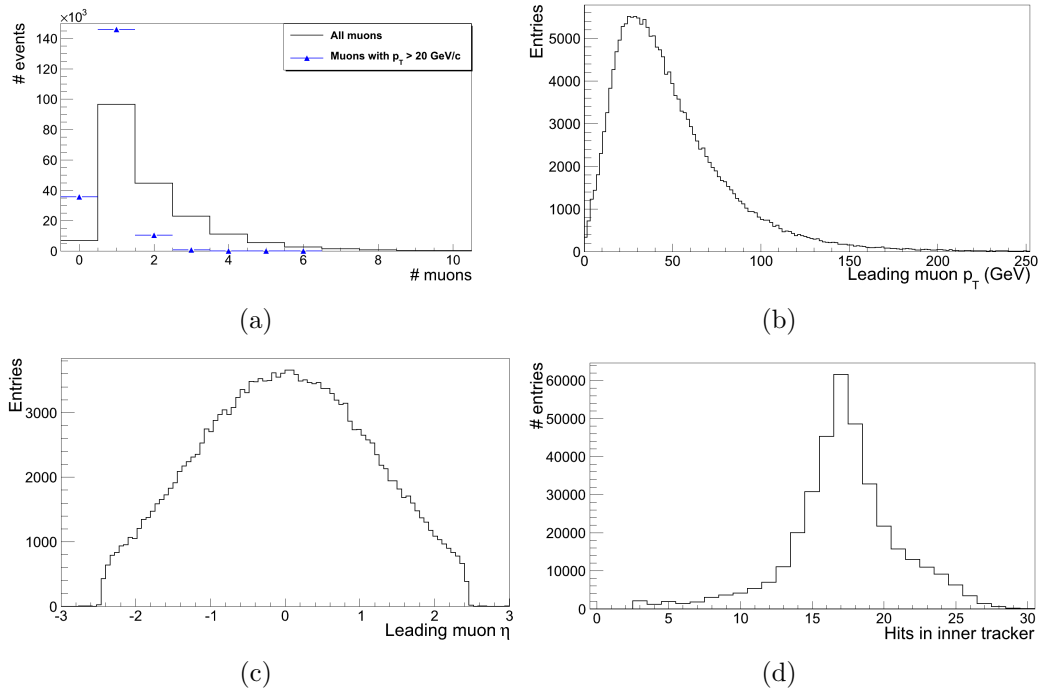


**Figure 3.2:** a) Number of muons (black line) and number of muons with  $p_T > 20$  GeV/c (blue triangles) in a semi-muonic  $t\bar{t}$  event. b-c) Transverse momentum and pseudo-rapidity of leading muon. d) Number of hits of the leading muon in the CMS detector.

### 3.3 b-flavour Identification

The presence of multiple jets in hadron collisions is a motivation to develop methods which identify, with some precision, the quark flavour from which the jet originates. Such a method can contribute to a better reconstruction and classification of the observed event.

In the case of a gluon or u-, d-, s-quark this is currently impossible but the high mass of the b-quark allows the identification of a jet originating from a b-quark. To a lesser extent this also holds for c-quarks which will however not be discussed further. The method to identify the b-flavour is called b-tagging or b-flavour identification. B hadrons are produced during fragmentation of

b-quarks and have a large lifetime, about  $1.568 \pm 0.009$  ps [1]. Hence they have a typical decay length of about  $450 \mu m$ , resulting in a displaced vertex observable by the CMS silicon tracker. Therefore a jet originating from a b-quark can be characterized by the presence of significantly displaced tracks with respect to the primary vertex, caused by the decay of the heavy B hadron as shown in Figure 3.3(a). This property is the main idea behind the impact parameter based b-tagging algorithm [38] used in this thesis.

The impact parameter is the distance between the primary vertex and the linearized track in the point of minimal distance between the track and the jet axis, as shown in Figure 3.3(b).

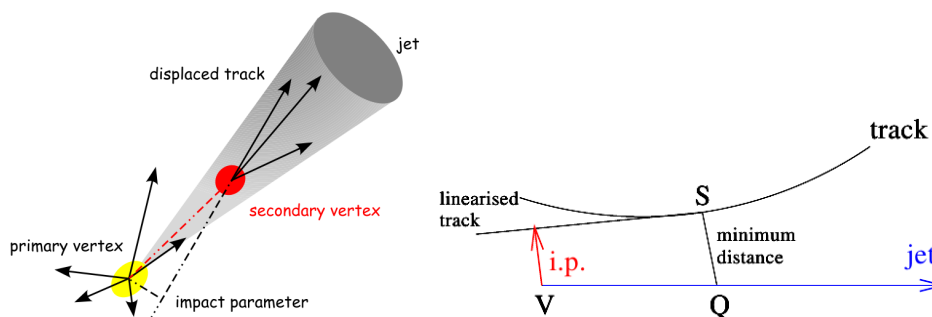


**Figure 3.3:** a) Schematic representation of a B-hadron decaying inside a b-jet. b) Geometrical interpretation of the impact parameter between the track and the primary vertex.

The impact parameter based b-tagging algorithm differentiates bottom quark jets from other jets by calculating a discriminating value or discriminator, which can be transformed into a probability of a jet to originate from a b-quark. This discriminator is defined as the three-dimensional impact parameter significance of the  $n$ -th track, where the tracks are ordered in descending impact parameter significance. If  $n = 2$  the algorithm yields a higher efficiency for selecting bottom jets while if  $n = 3$  the lower efficiency is compensated by a higher purity to select the bottom quark jet. The corresponding algorithms are respectively called high efficiency and high purity track counting b-tagging algorithm. In this thesis the high efficiency algorithm with  $n = 2$  will be used.

The discriminator distribution for both cases is given in Figure 3.4, which shows the possibility for the discriminator to be negative. This can be explained with Figure 3.3(b). If the point of minimum distance between the jet direction and the track lies after the interaction point, w.r.t. the traveled path of the jet with the interaction point as origin, the discriminator is given

a positive sign. A minimum distance point obtained before the interaction point results in a negative discriminator value. Since b-quarks decay after having traveled approximately  $450 \mu\text{m}$  a positive discriminator value is expected, which is indeed visible in Figure 3.4.

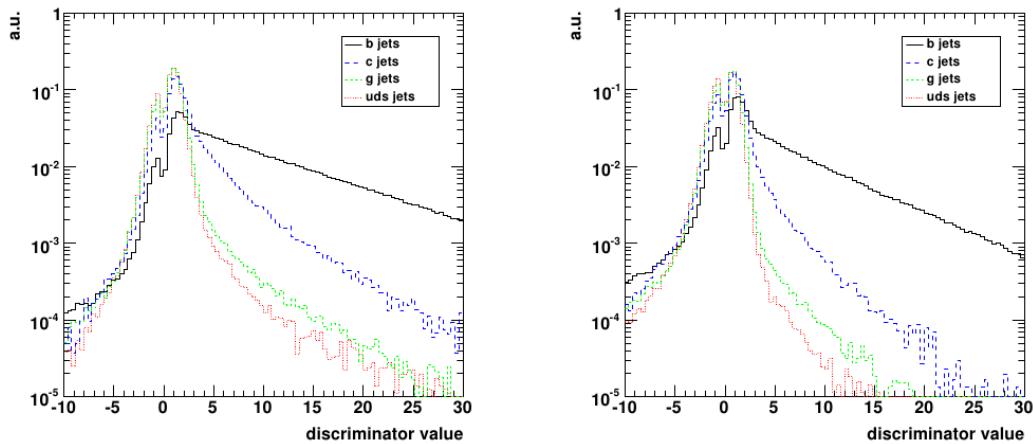


**Figure 3.4:** Discriminator value for the high efficiency (left) and high purity (right) track counting b-tagging algorithm for jets reconstructed in  $t\bar{t}$  events.

Based on Figure 3.4 the track counting b-tagging algorithms identify b-quark jets as those with a discriminator value higher than some specific threshold value. It is applied with different predefined threshold values, called *working points*. Some examples are presented in Table 3.1. These working points select all discriminator values larger than the corresponding discriminator cut value.

A higher threshold or working point value implies a lower mis-tag rate for the b-jets, but also a smaller amount of b-jets selected, hence a lower efficiency.

Working Point	Discriminator value	Mis-tag rate (%)
Loose	1.7	10
Medium	3.3	1
Tight	10.2	0.1

**Table 3.1:** Working points with the corresponding threshold on the discriminator value and mis-tag rate [39].

### 3.4 Missing Energy

The neutrinos produced in the decay of the W-boson in semi-muonic  $t\bar{t}$  events should be accurately reconstructed in order to rebuild the entire event topology. The difficulty belonging to the neutrino selection is the fact that the neutrino escapes the experiment undetected due to the very weak interaction with other particles, accounting for the name *Missing Energy*.

Nonetheless, the neutrino properties can be obtained by making the detector as hermetically closed as possible such that the interaction and properties of all other particles can be reconstructed precisely. Then, due to energy conservation between the initial and final state, any measured energy loss can be related to particles escaping detection.

In hadron colliders, such as the LHC, there is an extra challenge which renders the reconstruction of neutrinos even more difficult, namely that the kinematics of the constituents of the parton which take part in the hard collision are not known. Thus in contrary to lepton colliders, where the properties of the initial particles can be exactly identified, hadron colliders have only probabilistic information about the initial conditions summarized in the parton density functions. Since the hadrons travel along the beampipe, along the  $z$ -axis of the detector, the  $x$ - and  $y$ -components of the total momentum before the collision equals zero. Therefore hadron colliders focus on the transverse missing energy (MET), obtained as the compliment of the combined  $x$ - and  $y$ -component of the observed momenta in the final state.

An example of such a neutrino reconstruction in the transverse plane is given in Figure 3.5.

In this thesis the  $x$ - and  $y$ -component of the neutrino momentum are obtained by looking at the  $x$ - and  $y$ -momenta of the four leading jets and the isolated muon, hence the particle content expected for a semi-muonic  $t\bar{t}$  event.

The comparison of the reconstructed momentum with the momentum value from the simulated neutrino is given in Figure 3.6(a). It shows an equally reconstruction efficiency for the  $x$ - and  $y$ -component of the neutrino's momentum. This is expected since both components are obtained with a similar method.

Figure 3.6(b) the resolution on the transverse momentum of the neutrino is given, indicating a better resolution for low energy. This because a high-energetic neutrino implies an energetic complement, which has a lower reconstruction resolution due to radiation.

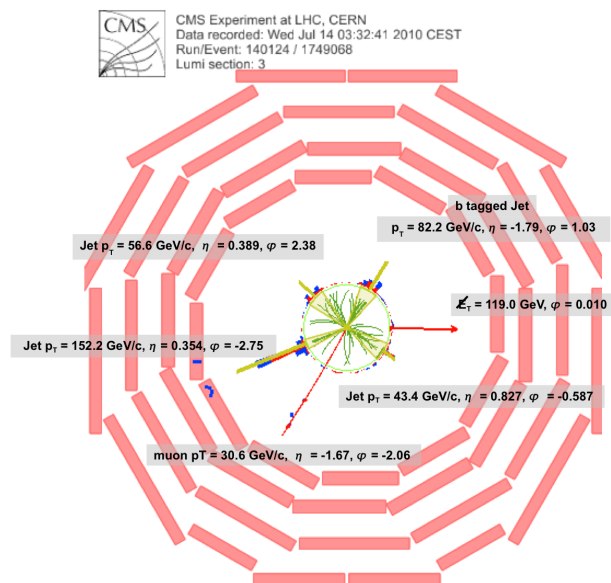


**Figure 3.5:** Representation of the reconstructed missing transverse energy in a top-pair candidate event in CMS [40].

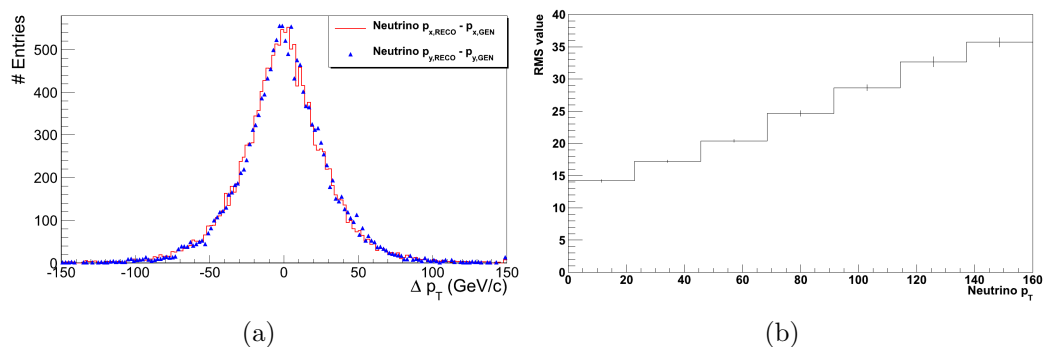


**Figure 3.6:** a) Comparison between the reconstructed and simulated  $p_x$  (red) and  $p_y$  (blue) momentum of the neutrino. b) Resolution on  $E_T$  as a function of the neutrino's  $p_T$ .

For this thesis also the much more difficult to reconstruct  $p_z$  component of the neutrino's momentum needs to be known. Namely because the W-boson in the relevant semi-muonic  $t\bar{t}$  events is obtained by combining the reconstructed information of the neutrino and the muon. Since collider experiments have only information about final state particles, intermediate particles such as the W-boson cannot be measured directly.

In this thesis the  $p_z$  value is obtained by introducing the W-boson mass constraint represented in Equation (3.2). Assuming neutrinos are massless this leads to a quadratic equation in terms of the neutrino  $p_z$  momentum component. This equation is only solved for a positive discriminant  $D^2$ , ensuring physical solutions.

$$m_W^2 = (E_l + E_\nu)^2 - (p_{x,l} + p_{x,\nu})^2 - (p_{y,l} + p_{y,\nu})^2 - (p_{z,l} + p_{z,\nu})^2 \quad (3.2a)$$

$$\begin{aligned} &= (E_l + \sqrt{p_{x,\nu}^2 + p_{y,\nu}^2 + p_{z,\nu}^2})^2 - (p_{x,l} + p_{x,\nu})^2 \\ &\quad - (p_{y,l} + p_{y,\nu})^2 - (p_{z,l} + p_{z,\nu})^2 \end{aligned} \quad (3.2b)$$

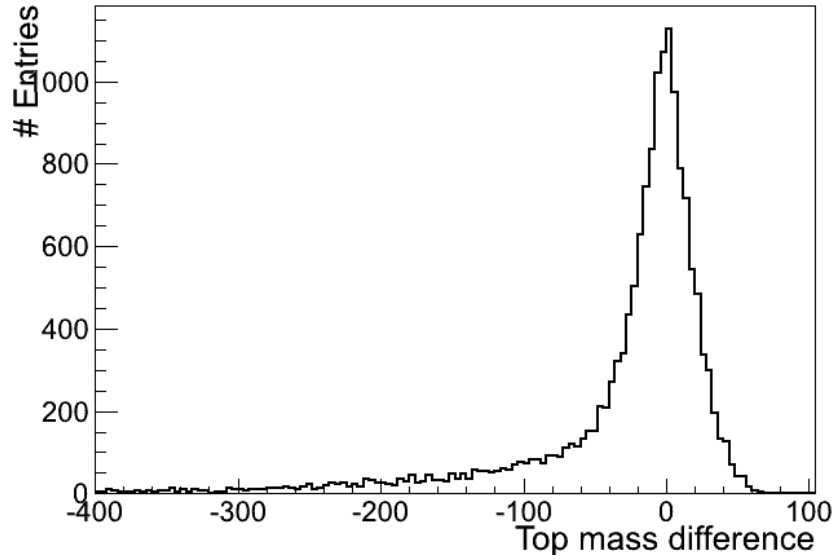
From the two possible solutions for the  $p_z$  component, the one which results in the best top quark mass value is selected. This is obtained by combining the neutrino, muon and bottom quark momenta from the leptonic top quark decay, is selected. The deviation from the top quark mass value is represented in Figure 3.7(a). It should be noted that this result is also affected by the reconstruction accuracy of the corresponding leptonic<sup>3</sup> b-quark and muon.

The precision of the used reconstruction method is shown in Figure 3.7(b), which contains the comparison between the obtained  $z$ -component of the neutrino momentum and the simulated value. Compared to  $x$ - and  $y$ -component reconstruction, the  $p_z$  distribution also peaks for deviations smaller than 100 GeV/c. The main difference between the distribution is the longer tail for the  $z$ -component, which is due to the complexity of the reconstruction method.

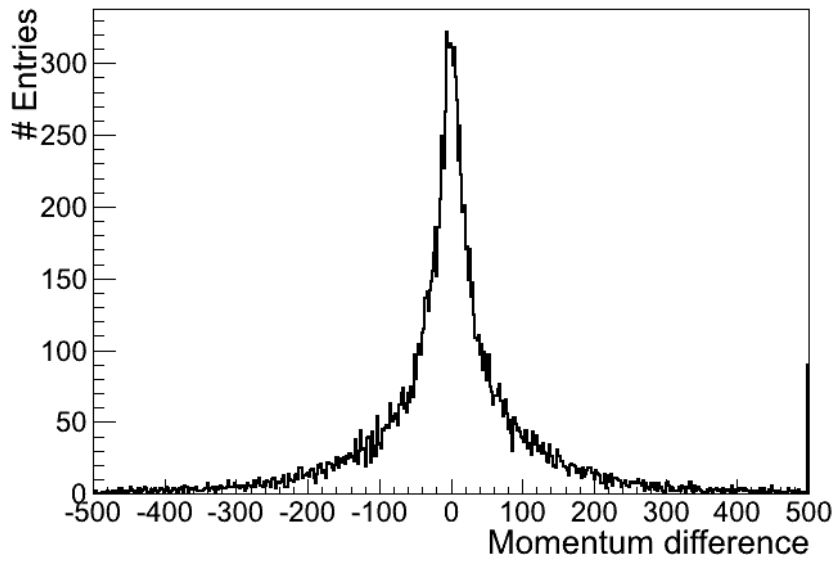
---

<sup>2</sup>Discriminator  $D$  is defined as  $D = b^2 - 4ac$  for the quadratic equation  $ax^2 + bx + c$  with solutions  $x_{\pm} = \frac{-b \pm \sqrt{D}}{2a}$ .

<sup>3</sup>A leptonic b-quark in this case indicates a b-quark produced by the leptonic decay top quark.



(a)



(b)

**Figure 3.7:** a) Comparison of top quark mass ( $173 \text{ GeV}/c^2$ ) with the value obtained from the reconstructed muon, leptonic b-quark and neutrino. b) Comparison between the reconstructed neutrino  $z$ -momentum and simulated.

# Chapter 4

## Selecting top-pair topologies

The previous chapter explained how the physics objects present in the final state of a hadron collision are reconstructed in the CMS detector. Once the final state of the event has been reconstructed, only the semi-muonic  $t\bar{t}$  signatures should be selected and studied in more detail to obtain a measurement of the W helicities.

A first step is done by the event selection algorithm which will select the physics processes of interest out of the enormous background. The following step consists of matching the selected jets with the quarks present in semi-muonic  $t\bar{t}$  topology such that the entire event topology is reconstructed. Only then the event properties can be examined.

### 4.1 Event Selection

The used event selection criteria, Selection Version SelV4 [42], are listed below. They are applied on the kinematic properties, the quality and the number of reconstructed objects in the events. The motivation for each applied cut will also be discussed.

- The event should pass the single muon High Level Trigger.
- At least one isolated muon with  $p_T > 20$  GeV/c and  $|\eta| < 2.1$  is required.
- At least four jets with  $p_T > 30$  GeV/c, after Level-2 + Level-3 and Level-1 + Level-2 + Level-3 + Level-2 Level-3 residual jet energy calibrations on simulation and data samples respectively, and  $|\eta| < 2.4$  are required.

The trigger selection is necessary since only a limited amount of events per second can be stored by the CMS experiment. Therefore only events containing single muons with  $p_T > 9$  GeV/c (data) and  $p_T > 15$  GeV/c (simulation) are kept for analysis. Events with lower transverse muon momentum give no indication for an interesting signal and are not essential for our study. This cut value changes with the instantaneous luminosity as is done for the 2010 data taking where starting from a specific run number, namely run number 147196 of 2010-RunB, the High Level Trigger only selects single muons with  $p_T > 15$  GeV/c.

In this thesis an additional pre-selection constraint of  $p_T > 20$  GeV/c and  $|\eta| < 2.1$  is required for the muons in all samples<sup>1</sup>.

A semi-muonic  $t\bar{t}$  event contains one muon with a large transverse momentum since it is produced in the decay of a W-boson. Therefore the demand of a transverse momentum higher than 20 GeV/c allows to distinguish between muons produced in other decays. The selected muons should be in the level-1 trigger acceptance, such that  $|\eta| < 2.1$  is asked in the event selection. Besides these two requirements, which are already demanded in the additional pre-selection of this thesis, the selected muons should pass a couple of quality cuts. The muon candidate has to be reconstructed as a Global Muon and a Tracker Muon. In the case of Global Muon it should be identified as a tight prompt global muon, implying a normalized  $\chi^2$  value, obtained from a fit on the muon path, smaller than 10 and at least one valid muon hit in the muon system. Also the silicon tracker should have at least 10 hits and minimum one pixel hit should be found for the muon candidate. A cut is applied on the absolute value of the impact parameter calculated with respect to the average beamspot, requiring  $d_0(Bsp) < 0.02cm$ . It is also demanded that the  $z$ -coordinate of the Primary Vertex of the event and the  $z$ -coordinate of the muon's inner tracker vertex lie within a distance smaller than 1 cm. To avoid the selection of muons from the hard process, and not emerging from decays in jets, the muon should be well separated from any jet in the event such that  $\Delta R(\mu, jet) > 0.3$ . Finally in at least two muon stations segments should be matched to a global muon, since the Drift Tubes need two segments to trigger for a muon candidate.

The muon in semi-muonic  $t\bar{t}$  events should be isolated since, in contrary to the muons in the enormous background, they are not produced during the

---

<sup>1</sup>This pre-selection is not applied on the semi-muonic  $t\bar{t}$  sample since this influences the reconstructed W helicity measurement as will be explained in Chapter 5. The considered QCD sample is muon-enriched, implying that only events with  $p_T^\mu$  are kept.

fragmentation process of heavy hadrons. Therefore the background muons are contained inside the jet of the heavy quarks while the muons produced in the W- and Z-boson decay are in general isolated.

The isolation of muons can be identified by combining two cones in the electromagnetic and hadronic calorimeter, one which measures the energy deposited by the muon and one which measures the deposited energy of the surrounding particles. The veto cone has an opening angle  $\Delta R$  equal of 0.07 and measures the muon's energy. The isolation cone then measures the energy deposited in the surrounding area, with an opening angle  $\Delta R = 0.3$ . Both cones are depicted in Figure 4.1, where the inner cone is the veto cone and the outer the isolation cone. From this Figure is clearly visible that the veto cone follows the muon direction and takes into account the effect of the magnetic field on the muon path. The isolation cone on the other hand is constructed from the muon direction at the vertex.

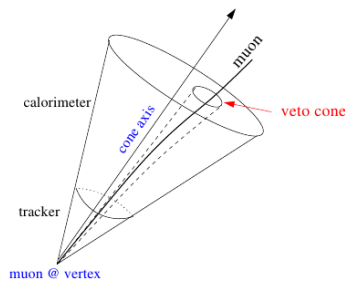


**Figure 4.1:** Isolation and Veto cone around a reconstructed muon.

Then the relative isolation, defined in Equation (4.1), can be used to reject the multi-jet background.

$$RelIso = \frac{\sum p_T^{tracks, iso-veto} + \sum E_T^{ECAL, iso-veto} + \sum E_T^{HCAL, iso-veto}}{p_T^\mu} \quad (4.1)$$

This because a relative isolation value around 0 indicates the presence of only the muon itself in the isolation cone. A large relative isolation value implies a lot of energy deposits in the isolation cone not coming from the muon and indicates a large activity around the muon. Therefore a relative isolation cut at 0.05 discriminates between the multi-jet background and the  $t\bar{t}$  events.

In order to avoid any overlap of the different top quark decay channels, two veto constraints are applied. The dilepton channel is excluded by rejecting all events containing an additional Global Muon with  $p_T > 10$  GeV/c,  $|\eta| < 2.5$  and  $RelIso < 0.2$ . The electron veto rejects events with an electron

with  $E_T > 15$  GeV/c,  $|\eta| < 2.5$  and  $\text{RelIso} < 0.2$  excluding the electron and dilepton channel.

Figure 4.2(a) indicates that the requirement of an isolated muon significantly reduces the QCD background. The other cuts applied in the muon part of the event selection can therefore be considered as quality cuts since they have a similar effect on all samples. After the muon selection the dominant remaining background is the W+jets and Z+jets samples since these events also contain an isolated high-energetic muon originating from the W-boson or Z-boson decay. Figure 4.2(b) gives the  $p_T$  distribution for the selected muon after the complete event selection.

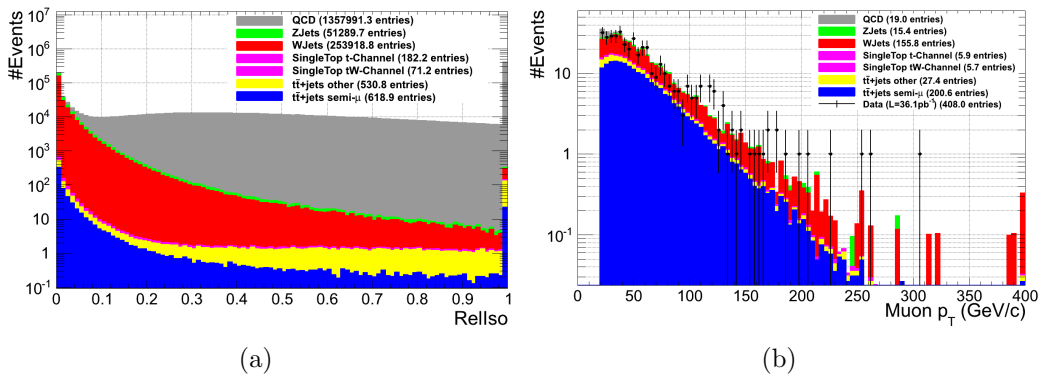


**Figure 4.2:** a) Relative isolation of muon before this constraint of the event selection has been applied. b) Transverse momentum of muon obtained after full event selection.

These histograms compare the data distribution against the complete background, scaled to the data luminosity. The different contributing backgrounds are QCD (gray), Z+jets (green), W+jets (red), both single top channels (pink), semi-muonic  $t\bar{t}$  (blue) and remaining  $t\bar{t}$  (yellow). The data is plotted as black dots with associated uncertainty bars.

The criterion for applying a cut of 30 GeV/c on the transverse momentum of the jets can be justified with Figure 4.3, which shows the  $p_T$  of the fourth leading jet<sup>2</sup> before and after the applied event selection. Besides the cuts on  $p_T$  and  $\eta$  the jets also should pass some quality cuts, namely different jet-ID requirements. These have been optimized to reduce the influence of noise from the calorimeter and keep the physical jets. The jet is required to

<sup>2</sup>The fourth leading jet is defined as the fourth jet in the selected jets, which are ordered in descending  $p_T$ .

have more than one constituent, to have CEF, NHF and NEF smaller than 0.99 and to have CHF and NCH larger than 0. The used abbreviations stand respectively for charged electromagnetic fraction, neutral hadron energy fraction, neutral electromagnetic fraction, charged hadron energy fraction and multiplicity of charged hadrons.

Figure 4.3(a) describes the  $p_T$  distribution for the fourth leading jet when only the High Level Trigger and full muon constraints are applied while Figure 4.3(b) gives the same distribution with also the jet criteria in the event selection. Comparing these two distributions indicates the enormous reduction of the  $W + \text{jets}$  background since these events rarely contain 4 high-energetic jets.

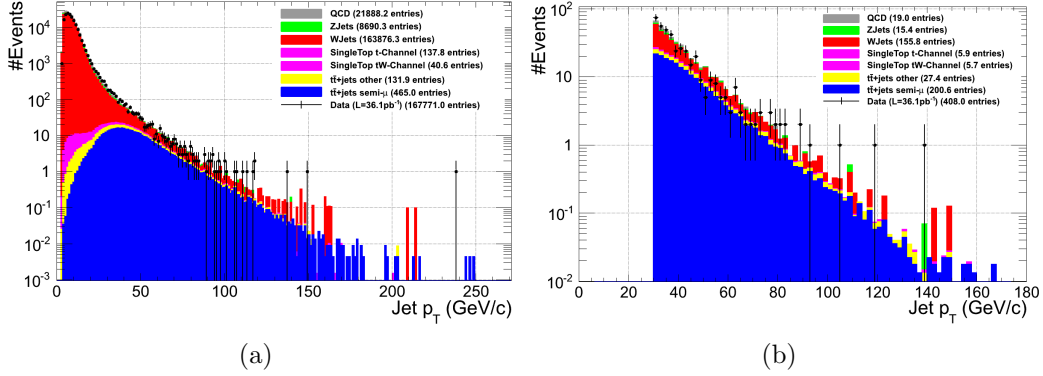


**Figure 4.3:** Transverse momentum of fourth leading jet without cut (left) and with  $p_T > 30$  GeV/c cut applied (right).

Table 4.1 gives the specific sensitivity of all the used samples for the different event selection steps and summarizes the above explained observations. The obtained percentages support the used event selection since the irrelevant processes have been removed substantially while the relevant process, semi-muonic  $t\bar{t}$ , is still present. The procentual loss for the subsequent selection constraints can be easily understood with the corresponding event topology and indicates the importance of the distinct steps used in the event selection.

In order to compare the simulated events with the data, all samples should be scaled towards the data luminosity. The corresponding values for all samples are given in Table 4.2. It is expected that the sum of all simulations for this luminosity should equal the data values, hence no percentages but

	<b>Initial</b>	<b>muon (<math>p_T &gt; 20</math>)</b>	<b>4 jets (<math>p_T &gt; 30</math>)</b>
$t\bar{t}$ semi- $\mu$	193038	54.71 %	23.60 %
$t\bar{t}$ other	155627	19.96 %	4.09 %
<b>single t (tW Channel)</b>	105554	51.62 %	7.28 %
<b>single t (t Channel)</b>	131151	70.79 %	2.98 %
<b>Z + jets</b>	649727	30.38 %	0.04 %
<b>W + jets</b>	2671533	80.53 %	0.06 %
<b>QCD</b>	8348714	1.35 %	0.001 %
<b>Data</b>	1640742	11.23 %	0.02 %

**Table 4.1:** Percentage of remaining events for the different cuts used in the event selection. The values given for the initial situation represents the pre-selection situation, except for the semi-muonic  $t\bar{t}$  sample. The muon constraint includes both the second muon and electron veto.

scaled values are represented.

	<b>Initial</b>	<b>muon (<math>p_T &gt; 20</math>)</b>	<b>4 jets (<math>p_T &gt; 30</math>)</b>
$t\bar{t}$ semi- $\mu$	654.1	438.7	189
$t\bar{t}$ other	640.5	124.7	25.8
<b>single t (tW Channel)</b>	78.8	40.7	5.7
<b>single t (t Channel)</b>	197.8	140.0	5.9
<b>Z + jets</b>	27 154.8	8 248.9	11.7
<b>W + jets</b>	197 075.2	158 766.2	116.3
<b>QCD</b>	856 297.1	11 513.9	9.1
<b>Total Simulation</b>	1 082 098.3	179 273.1	363.5
<b>Data</b>	1 640 742.0	184 211.0	408.0

**Table 4.2:** Number of remaining events for the different constraints used in the event selection with scaled luminosity. The values given for the initial situation represents the pre-selection situation, except for the semi-muonic  $t\bar{t}$  sample. The muon constraint includes both the muon and electron veto.

From this table is clear that in the initial situation the amount of data events is larger than described by the simulated events. Even with the ex-

pected uncertainty of 12 % on the total simulation, simulation cannot be compared against data. This can be understood since the used simulated samples have been selected to describe the data sample after the complete event selection. Hence before the application of any quality requirements, more simulated samples are needed to have an agreement.

When only the muon selection cuts have been applied simulation and data can be considered being equal, including the uncertainty on simulation. This is expected since the considered simulation samples are chosen to describe or influence semi-muonic  $t\bar{t}$  events. Hence an isolated muon signal is expected. In the final column simulation and data lie inside the uncertainty region, but have no excellent match. This discrepancy was studied in detail, and thoroughly explained in [43]. In order to obtain correct results, scale factors  $\beta$  should be introduced which has to be applied to the predicted cross section of a given process to derive the measured cross section. These scale factors, together with the corrected cross sections and number of simulated events can be found in Table 4.3.

	Scale factor	Measured cross section (pb)	Events
$t\bar{t}$ semi- $\mu$	1.06	24.7	200.6
$t\bar{t}$ other	1.06	142.2	27.4
single t (tW Channel)	1.0	10.6	5.7
single t (t Channel)	1.0	20.93	5.9
Z + jets	1.32	4 023.4	15.4
W + jets	1.34	41 960.8	155.8
QCD	2.09	176 979.7	19.0
<b>Total Simulation</b>			429.8
<b>Data</b>		36.1389	408.0

**Table 4.3:** Scale factors, measured cross section and associated event number for the different simulation samples, scaled to the data luminosity. Scale factors ensure a simulation prediction compatible with data measurement. The measured cross section is obtained by multiplying the theoretical cross section with the scale factor.

The event numbers given in Table 4.3 are not the ones which will be used further in this analysis, since the effect of the neutrino reconstruction has not been incorporated. The associated values can be found further, namely in Table 5.3.

## 4.2 Jet-quark matching algorithm

Once the relevant event topology has been selected and the background contribution is reduced, the full topology of the semi-muonic  $t\bar{t}$  event should still be reconstructed. The main difficulty consists of matching the four measured leading jets with the correct corresponding quarks present in the event topology.

The jet-quark matching algorithm that will be used in this thesis is an event-by-event  $\chi^2$  method. The  $\chi^2$  value is defined in Equation (4.2) for the three jets originating from the hadronical decaying top quark, with  $t \rightarrow j_3 W \rightarrow j_3 j_2 j_1$  used as convention.

$$\chi^2 = \frac{(m_{j_1 j_2} - \hat{m}_W)^2}{\sigma(\hat{m}_W)^2} + \frac{(m_{j_1 j_2 j_3} - \hat{m}_{top})^2}{\sigma(\hat{m}_{top})^2} \quad (4.2)$$

The used constraints are the top quark and W-boson masses, respectively  $\hat{m}_{top} = 173.04 \text{ GeV}/c^2$  and  $\hat{m}_W = 82.90 \text{ GeV}/c^2$ . The constraints are not applied on the total event, including the b-quark associated with the leptonical decaying top quark, since the reconstruction of the neutrino is not efficient enough to provide a correct matching.

These mass values, together with the mass resolution used to rescale the mass differences, are obtained by applying a Gaussian fit to the mass distribution for simulated semi-muonic  $t\bar{t}$  events. The obtained resolutions are  $\sigma = 18.06 \text{ GeV}/c^2$  and  $\sigma = 11.04 \text{ GeV}/c^2$  for the top and W-boson mass respectively. This illustrates that relatively the top quark mass is equally well reconstructed compared to the mass of the W-boson, namely approximately 11 % resolution. Hence both terms contribute equally in the  $\chi^2$  expression.

Normally the four measured jets can be matched with these three quarks in 24 different ways, but only 12 different configurations need to be considered since the interchange of the two jets originating from the W-boson is not relevant for the analysis described in this thesis. The used jet-quark matching algorithm then calculates for all twelve possibilities the  $\chi^2$  value and selects the jet-quark matching with the best reconstructed top quark and W-boson masses, and thus lowest  $\chi^2$ .

The obtained  $\chi^2$  distribution for the best reconstructed configuration is given in Figure 4.4 and shows the expected behavior, namely a large peak at low  $\chi^2$  values and a long tail.

Once the jets have been matched with a specific quark, the properties and efficiency of this topology reconstruction can be investigated. An interesting property is the reconstructed W-boson and top quark mass distribution,

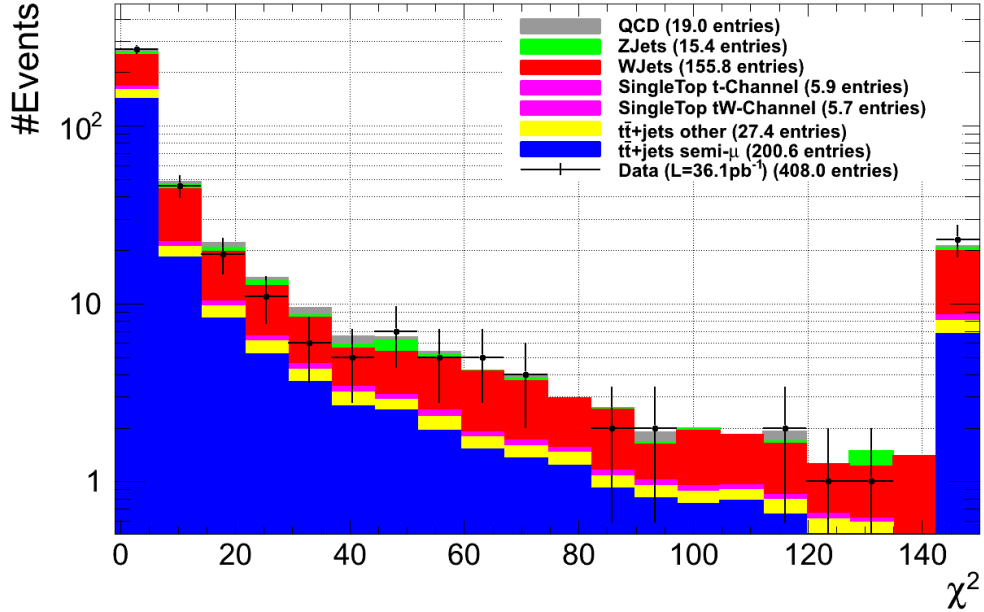


**Figure 4.4:** Distribution of the best of twelve  $\chi^2$  values obtained from the used jet-quark matching algorithm with W-boson and top quark mass as constraints.

which should peak around the fitted mass values,  $\hat{m}_W$  and  $\hat{m}_{top}$ . Figure 4.5 indeed shows these peaks, but also a significant tail of wrong jet-quark configurations. The possibility to correctly reconstruct the W-boson and top quark mass can be represented by the width of the obtained distribution. For this a Gaussian is fit onto the mass distribution for semi-muonic  $t\bar{t}$  events, only for a limited range in order to avoid contributions from the tail. The fitted values are  $20.55 \pm 1.84$  and  $11.57 \pm 1.03$  for the W-boson and top quark mass distribution respectively. These results are in agreement with the resolution values obtained from simulated semi-muonic  $t\bar{t}$  events.

An accurate efficiency of the used  $\chi^2$  method can only be obtained by comparing the reconstruction for simulated semi-muonic  $t\bar{t}$  events with the correct configuration. Hence the rest of this section concerning the jet-quark matching algorithm only looks at such simulated semi-muonic  $t\bar{t}$  events. Table 4.4 gives the percentages that the  $\chi^2$  algorithm matches a reconstructed jet with the associated quark. This table shows that the quarks originating from the hadronical decaying W-boson have the lowest matching efficiency, explained by the fact that two jets should be well reconstructed. The difference between the hadronic and leptonic b-jet is influenced by multi-

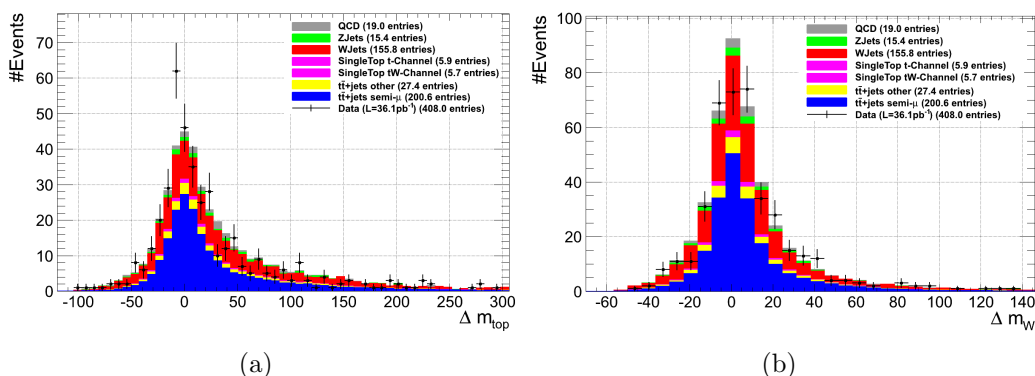


**Figure 4.5:** Top quark(a) and W-boson (b) mass distribution obtained with the reconstructed quarks originating from the hadronic decaying top quark. The distribution gives an indication of the efficiency of the used  $\chi^2$  method as jet-quark matching algorithm.

ple effects, one of them being the activity around the jet. The hadronic b-jet is produced together with the jets originating from the hadronic decaying W-boson, making reconstruction of the jet much more difficult. The leptonic b-jet on the other hand is more isolated and thus less influenced by other jets. Another important effect comes from the mass constraints required for the  $\chi^2$  matching method. The hadronic b-quark is only selected when the top quark mass is properly reconstructed while the leptonic b-quark is considered as the remaining fourth jet in the event. Hence the hadronic b-jet matching is heavily influenced by the reconstruction efficiency of the quarks originating from the hadronic W-boson.

Correct leptonic b-jet	38.99 %
Correct hadronic b-jet	32.19 %
Correct W hadronic quarks	27.45 %
Four jets correct	15.10 %

**Table 4.4:** Percentage of correct jet configuration.

In order to better understand the used  $\chi^2$  method Figure 4.6 is considered. It gives the percentage for the four quarks present in semi-muonic  $t\bar{t}$  events of being the first, second, third, fourth or higher jet in the  $p_T$  descending ordered selection. Also the fraction that the associated jet is not present in the event is shown.

It indicates a relatively equal reconstruction percentage for both the b-quarks and the highest  $p_T$  quark from the hadronic decaying W-boson. Since the quarks originating from the W-boson can be interchanged one is always defined as the highest  $p_T$  quark, explaining the large difference between these two quarks shown in Figure 4.6.

The obtained distribution corresponds to the expected, namely the jets belong most of the time to the four selected jets and thus only a small fraction is seen in the last two bins. The lowest  $p_T$  quark originating from the W-boson decays is an exception, namely about half of the time this jet is not selected. Hence the transverse momentum of this jet is often too low to pass the event selection.

The jet not being present in the event, and thus falling into the last bin, implies the missing jet either fails the minimum  $p_T$  criterion or another jet ID requirement or the missing jet falls into a region outside the geometrical acceptance of the detector.

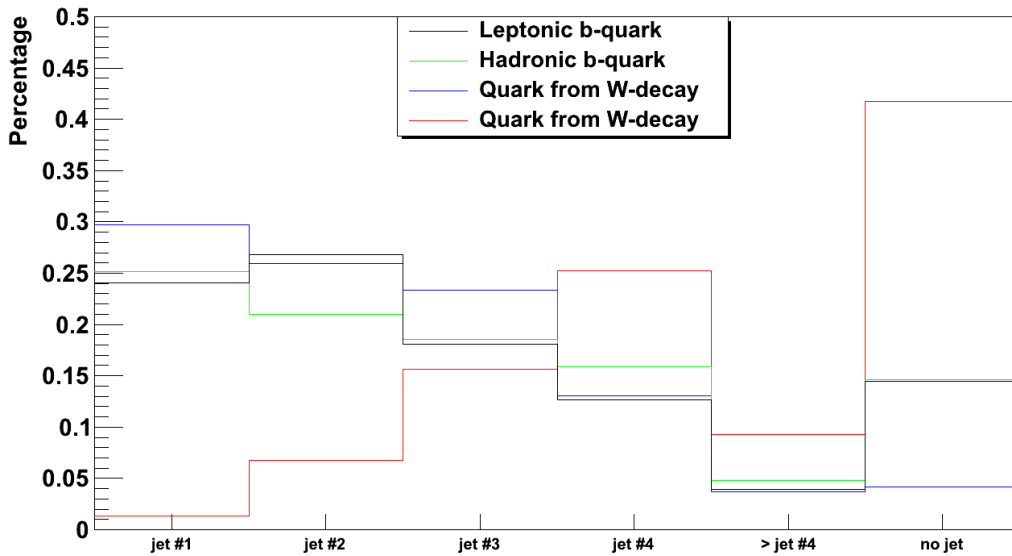


**Figure 4.6:** Percentage for the ordering of the different jets for simulated semi-muonic  $t\bar{t}$  events.

# Chapter 5

## Helicity distribution reconstruction

This analysis makes use of the reconstructed decay angle  $\theta^*$ , defined as the angle between the muon in the W-boson restframe and the W-boson in the top quark restframe. Therefore the four-momenta of the W-boson decaying into a charged muon and corresponding neutrino as well as of the b-quark from the parent top quark need to be properly reconstructed. This was achieved by the minimal  $\chi^2$  jet-quark matching algorithm as described in the previous chapter and leads to the distribution given in Figure 5.1.

This chapter explains how the obtained  $\cos\theta^*$  distribution can be optimized since, due to reconstruction and acceptance effects, this angular distribution gets distorted. Therefore in this thesis, the helicity distribution at parton level will be used for the event-by-event reweighting algorithm in order to obtain helicity distributions for alternative helicities.

### 5.1 Differential cross section and helicities

The differential cross section describing the angular distribution is given in Equation (5.1) with a left-handed  $f_-$ , longitudinal  $f_0$  and right-handed  $f_+$  contribution. The coefficients associated to each helicity value are obtained with the assumption that the sum of the three helicity values equals one.

$$\frac{d\sigma}{d\cos\theta^*} = f_- \frac{3(1 - \cos\theta^*)^2}{8} + f_0 \frac{3(1 - \cos^2\theta^*)}{4} + f_+ \frac{3(1 + \cos\theta^*)^2}{8} \quad (5.1)$$

In this thesis the differential cross section was reconstructed using the semi-muonic  $t\bar{t}$  simulated sample, since the obtained distribution should cor-

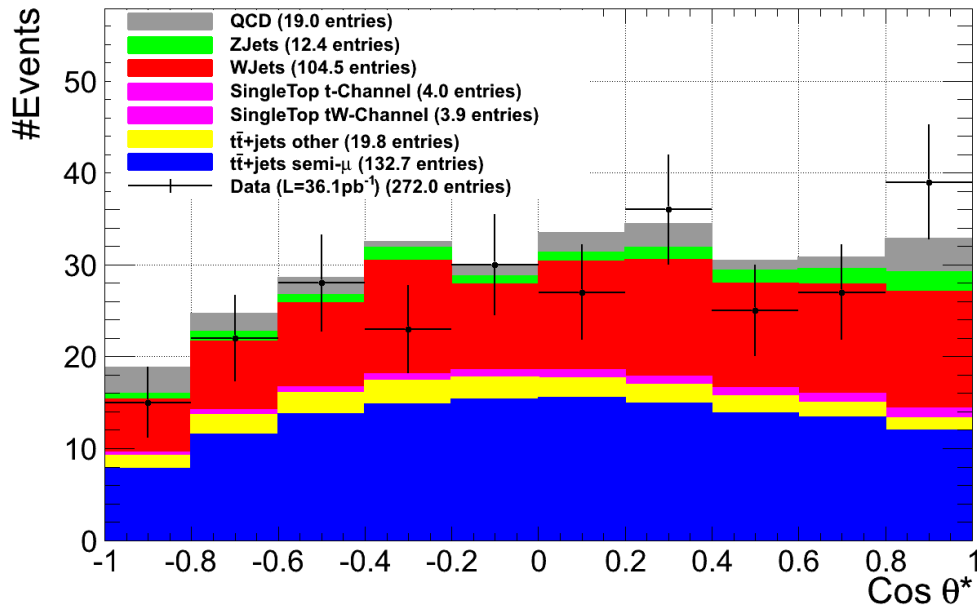


**Figure 5.1:** Helicity distribution obtained by the reconstruction of  $\cos \theta^*$  for all simulated samples and compared against the data distribution.

respond to the Standard Model distribution. This semi-muonic  $t\bar{t}$  sample contains namely the events which have the correct event topology to obtain the W helicity information. All the other simulated background samples are needed to ensure that the data sample, which contains all the events collected in the CMS detector, is correctly described.

The obtained results indicate that both the event selection and the reconstruction has a considerable effect on the helicity distribution. Therefore in this thesis the theoretical helicity distribution will be reconstructed on parton or generator level before any event selection has been applied. Even the preselection constraints for the semi-muonic  $t\bar{t}$  sample discussed in the previous chapter have been removed in order to have the best possible agreement with the Standard Model.

The different effects on the helicity distribution and motivation for the used reconstruction will be discussed in detail.

For all the events of the semi-muonic  $t\bar{t}$  simulated sample the decay path is reconstructed from the final state particles up to the initial top quarks such that the correct particles get reboosted in the correct restframe. This algorithm uses the initial sample without any quality constraints applied. The obtained helicity distribution is compared against the theoretical helicity distribution which gives best-fit values for the three W-boson helicity values.

These values are given in Table 5.1 together with the expected Standard Model helicity polarization values. The fitted helicity values will be further used in this analysis.

The visible deviation from the Standard Model values cannot be used to conclude that the weak interaction of the Standard Model is not a true V-A theory.

	Right-handed ( $f_+$ )	Longitudinal ( $f_0$ )	Left-handed ( $f_-$ )
Standard Model	$4.1 \times 10^{-4}$	0.698	0.301
Semi- $\mu t\bar{t}$	$0.033 \pm 0.055$	$0.642 \pm 0.137$	$0.324 \pm 0.100$

**Table 5.1:** Right-handed, longitudinal and left-handed helicity values for the Standard Model and obtained with the used simulated semi-muonic  $t\bar{t}$  sample.

With the obtained helicity values the contribution of the three different W-boson helicities can be represented. This is done in Figure 5.2. Contrary to the theoretical Standard Model distribution, the distribution shown in this figure does not converge to 0 for  $\cos\theta^*$  equal to 1. This difference is due to the relative high right-handed contribution, which is only significant in the angle range of  $-45^\circ$  to  $45^\circ$  corresponding to a  $\cos\theta^*$  range between 0.7 and 1.

The need of reconstructing the helicity distribution before any selection constraints have been applied can be easily understood. Since the Standard Model distribution is obtained from the weak V-A theory it does not incorporate momentum constraints.

The effect of the event selection on the helicity distribution on generator level is shown in Figure 5.3 which indicates a significant difference for  $\cos\theta^*$  smaller than  $-0.5$ . This follows from the definition of the helicity angle<sup>1</sup>. A  $\cos\theta^*$  value around  $-1$  implies a configuration where the muon is very close with the b-quark originating from the W-boson decay. Since the applied muon selection requires an isolated muon, the configurations with the muon and the b-quark traveling in the same direction will often be rejected. Therefore with an applied event selection it is expected to measure less events with a  $\cos\theta^*$  value around  $-1$ , an effect which is indeed visible in Figure 5.3.

<sup>1</sup>A schematic overview was given in Figure 1.2(a) in subsection 1.3.1.

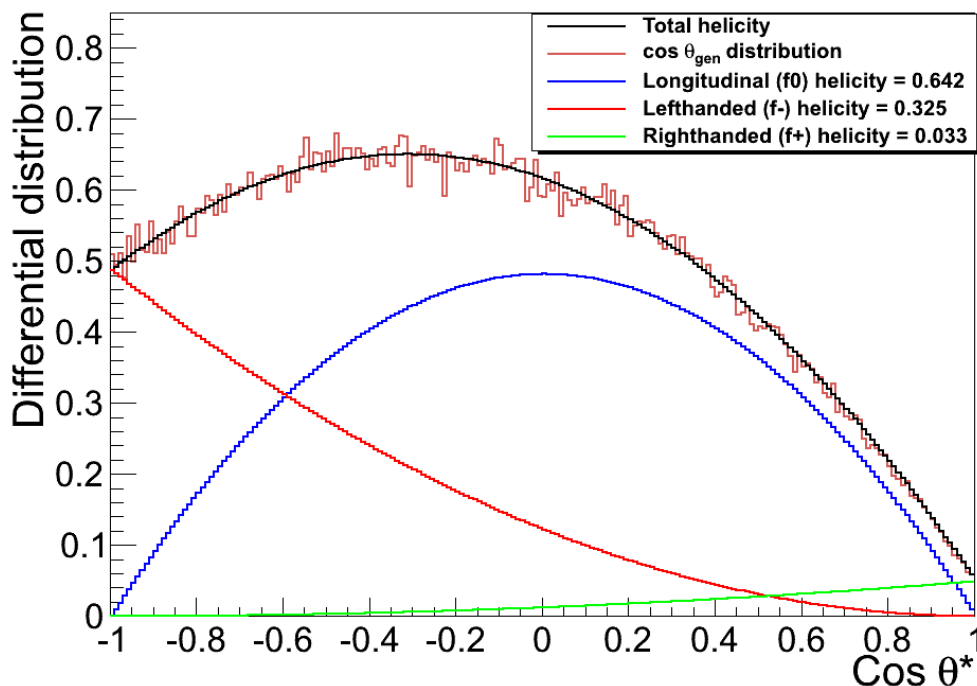


**Figure 5.2:** Theoretical helicity distribution for left-handed (red), right-handed (green) and longitudinal (blue) W-boson polarization with the obtained helicity values. The solid black line indicates the overall angular distribution and is fitted onto the reconstructed semi-muonic  $t\bar{t}$  helicity distribution.

That the event selection effect is mainly due to the muon constraints can be understood from Figure 5.4 which describes the helicity distribution after the different event selection constraints discussed in Chapter 4.1. Only the range with the largest deviation in Figure 5.3 is shown since otherwise the differences were not visible. It clearly indicates that the muon selection constraint has a considerable effect while the other selection steps, applied electron and muon veto and jet constraints, have almost no influence on the helicity distribution.

Figure 5.5 shows the effect of the reconstruction of the physics objects on a data-driven way. This means that the simulated semi-muonic  $t\bar{t}$  sample is considered as data without prior knowledge about the studied event. From this it is clear that the reconstruction has a considerable effect on the helicity distribution in the  $\cos\theta^*$  larger than 0.5. This implies a  $\theta^*$  value around 0 such that the associated configuration corresponds with the neutrino in the same direction as the b-quark.

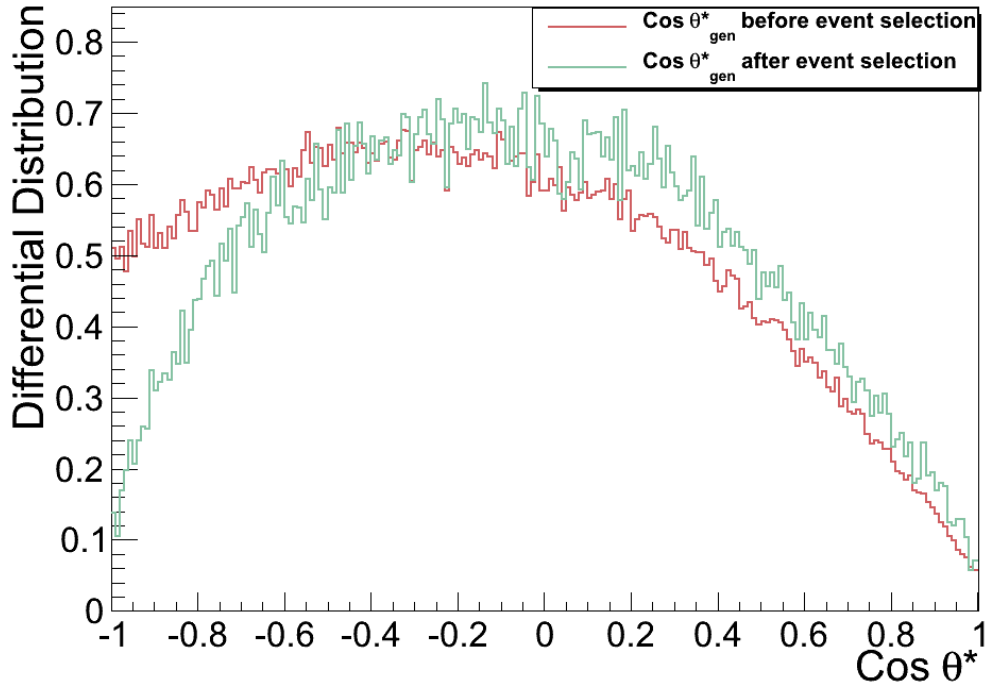


**Figure 5.3:** Helicity distribution for semi-muonic  $t\bar{t}$  events on generator level before applied event selection (red) and after complete event selection (green). The difference for  $\cos \theta^*$  is due to the requirement of isolated muons.

The observed distortion can be explained with the reconstruction efficiency of the b-quark, neutrino and muon. This is shown in Figure 5.6, which describes the helicity distribution obtained on a data-driven way for the semi-muonic  $t\bar{t}$  sample together with the helicity distribution with one of the particles reconstructed on generator level. Figure 5.6 clearly shows that the correct reconstruction of the b-quark and the neutrino has a large influence while the muon reconstruction has almost no effect. This can be understood by the different resolutions for the b-quark, neutrino and muon. Both the b-quark and neutrino have a bad resolution while the muon can be measured very accurately.

A possible explanation for the helicity distribution distortion for the specific  $\cos \theta^*$  values can be found in the corresponding angle configurations.

The above indicates that the reconstruction of the physics objects with the used minimal  $\chi^2$  jet-quark matching algorithm is of crucial importance. Since the muon is not affected by the used minimal  $\chi^2$  reconstruction method, it is comprehensible that the muon reconstruction has no significant effect on the helicity distribution.

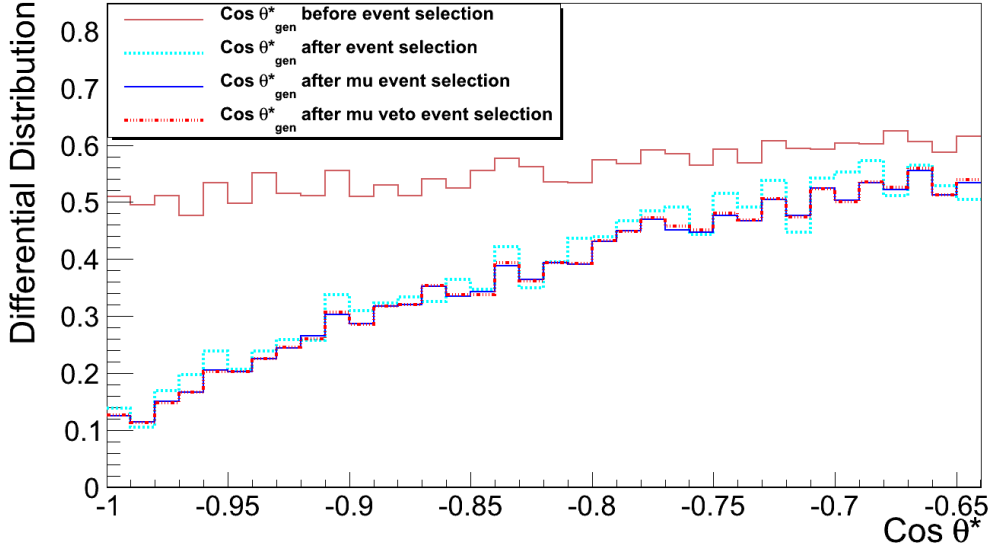


**Figure 5.4:** Effect of the different steps of the event selection on the helicity distribution of semi-muonic  $t\bar{t}$  events. The full red line represents the distribution before any applied event selection, also no pre-selection has been applied. The full blue line describes the distribution after the cut on muon  $p_T$  and the requirement of isolation. For the dashed red line also the muon and electron veto has been included in the event selection. The dashed blue line is the distribution after the complete event selection.

With all the individual aspects explained, Figure 5.7 represents the complete effect of resolution on the reconstruction. It shows the difference between the  $\cos\theta^*$  value obtained on generator level with the value obtained with a data-driven reconstruction. From Figure 5.7 is visible that most of the events are properly reconstructed, but that a smearing appears due to the presence of bad reconstructed events. This can be explained with a pseudo-experiment which generates two completely unrelated quantities<sup>2</sup> between  $-1$  and  $1$ . The difference between such values is also represented in Figure 5.7, which indicates that the performed reconstruction results in better results than a random angular distribution between  $-1$  and  $1$ . The smearing is also influenced due to the finite resolution of the detector. This effect can be eliminated with an unfolding technique [44], but is not done in this analysis. The resolution for the reconstruction is obtained with a Gaussian fit applied onto a limited  $\Delta\cos\theta^*$  region in order to exclude any influence from the smearing of bad reconstructed effects. The considered region was  $\Delta\cos\theta^*$

<sup>2</sup>Such a configuration corresponds to a badly reconstructed  $\cos\theta^*$  which contains no information about the original value.

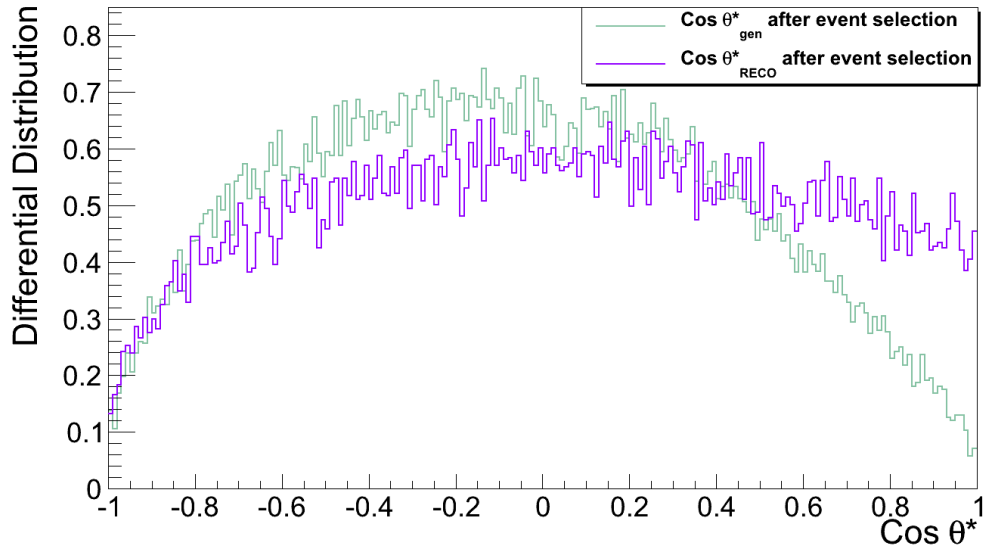


**Figure 5.5:** Helicity distribution for semi-muonic  $t\bar{t}$  events reconstructed on generator level (green) and on data-driven level (purple).

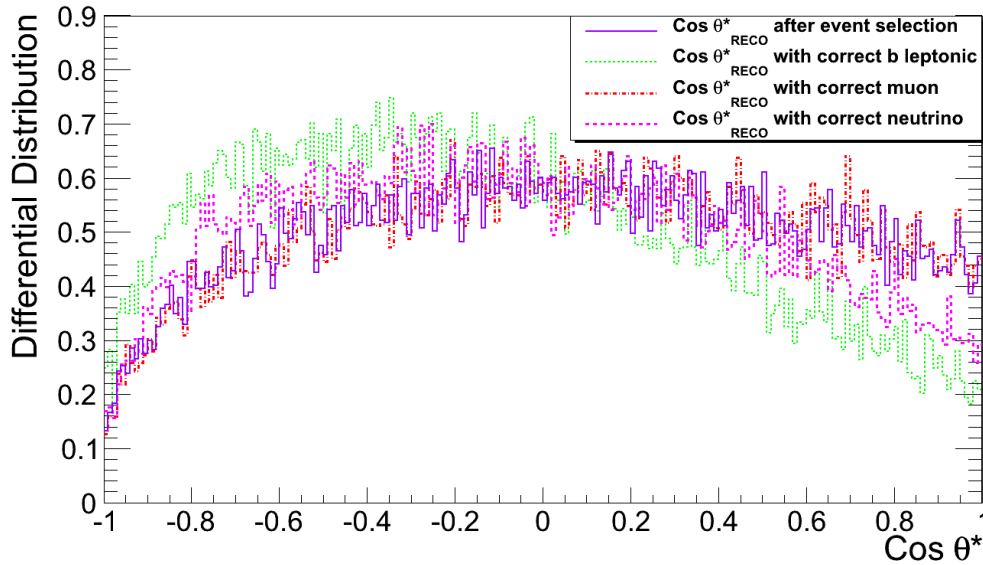


**Figure 5.6:** Effect of reconstruction on semi-muonic  $t\bar{t}$  helicity distribution. Distribution for complete event reconstruction (purple) and for reconstruction with one particle obtained on parton level is shown, respectively the muon (dashed red), neutrino (dashed pink) and b-quark (dashed green).

between  $-0.3$  and  $0.3$ , resulting in a resolution of  $0.235$ .

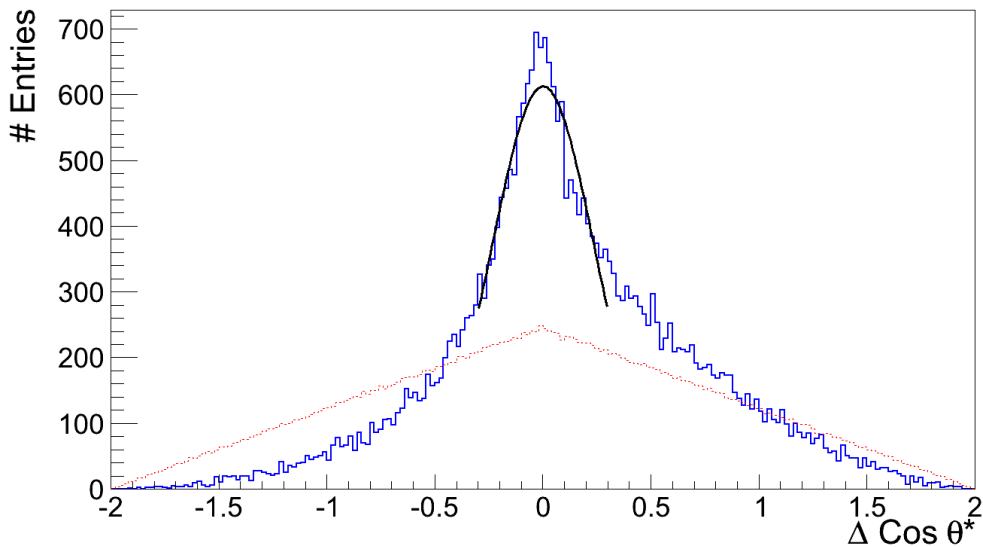


**Figure 5.7:** Difference between  $\cos\theta^*$  on generator level and after reconstruction for every semi-muonic  $t\bar{t}$  event (blue) together with the difference between two complete unrelated quantities (red). The Gaussian fit (black) applied onto a limited range gives a resolution of 0.235.

## 5.2 Reweighting expected helicity distribution

In this thesis the obtained helicity distribution for the data sample will be compared against the simulated helicity distribution for different helicity configurations. Then the distributions with the best match will represent the values of the W-boson helicity which describe the Wtb interaction most accurately. A deviation from the expected Standard Model values would be an indication of new physics.

The helicity distributions for different helicity configurations can be obtained on two different ways. One possibility is to simulate samples with an initial helicity configuration differing from the Standard Model, a method which demands lots of computer time and is not so straightforward as first expected. In this analysis the different helicity configurations are obtained by an event-by-event reweighting algorithm which uses the helicity distribution of the semi-muonic  $t\bar{t}$  sample before event selection and reconstruction as reference value.

The used reweighting algorithm compares for each event of the semi-muonic  $t\bar{t}$  sample the differential distribution value obtained with  $\cos\theta^*$  on

generator level for the used alternative helicity values against the Standard Model differential distribution on generator level, as defined in Equation (5.2). This weight is then applied onto the reconstructed  $\cos\theta^*$  value such that for each event the difference between the Standard Model and the alternative configuration gets incorporated in the corresponding distribution. The reweighting is only applied on the semi-muonic  $t\bar{t}$  sample since the other samples are not expected to contain any information about W-boson helicities. Hence the use of alternative helicity values should have no influence on these samples.

$$w = \frac{g(\cos\theta_{gen}^*|\vec{f}_{alt})}{g(\cos\theta_{gen}^*|\vec{f}_{MG})} \quad (5.2)$$

The effect of the reweighting on the reconstructed  $\cos\theta^*$  distribution is represented in Figure 5.8. It contains the Standard Model distribution and distributions with alternative helicities which have been adjusted with the event-by-event reweighting algorithm. This reweighting algorithm clearly has the expected effect.

The figure shows that the distribution with helicities values of 0.25, 0.65, 0.10 for the right-handed, longitudinal and left-handed polarization respectively gets increased in the  $\cos\theta^*$  equal to 1 region since the right-handed contribution is larger than for the Standard Model. Due to smaller left-handed helicity the distribution is decreased in the  $\cos\theta^*$  around  $-1$  region.

The 0.03, 0.35, 0.62 distribution on the other hand has a very large contribution from the left-handed helicity combined with an overall lowering due to the smaller longitudinal helicity.

### 5.3 Application of b-tagging

The events needed to study the W-boson helicities all contain a b-quark originating from the decay of the top quark, such that the impact of b-tagging could have a positive impact on the measurements. The large effect of the leptonic b-quark reconstruction efficiency on the helicity distribution shown in Figure 5.6, indicates the importance of an accurate reconstruction of the b-quark.

Therefore a track counting high efficiency b-tagging algorithm was applied for the Loose and Medium working points, respectively a discriminator value larger than 1.7 and 3.3.

In this thesis the used working point was determined by comparing the Standard Model distribution with two distributions with changed helicity values

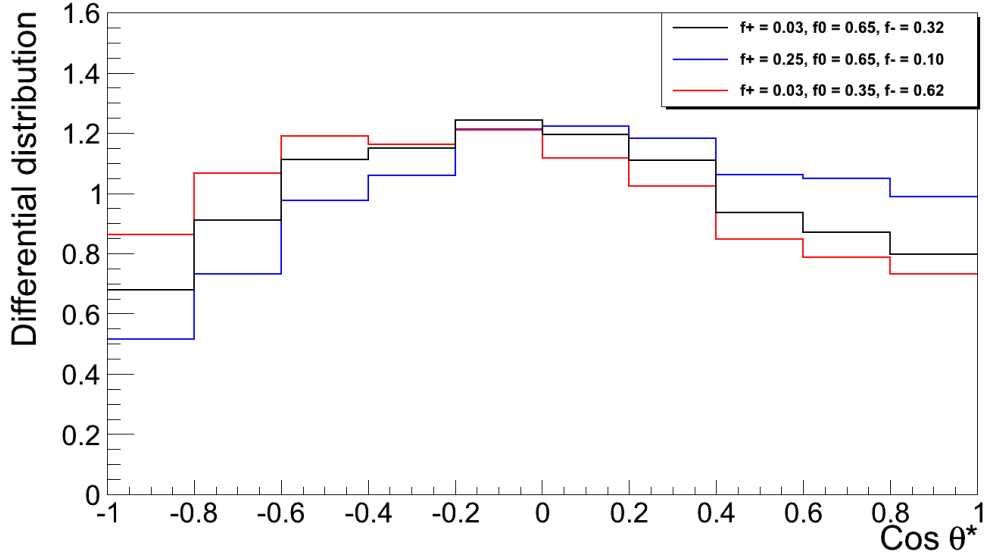


**Figure 5.8:** Effect of event-by-event reweighting algorithm on helicity distribution compared with the Standard Model distribution (black curve).

for the semi-muonic  $t\bar{t}$  sample. These alternative helicity values have a horizontal or vertical change in the  $(f_+, f_0)$  plane compared to the Standard Model value, as shown in Figure 5.9. The comparison is done with a  $\chi^2$  method represented in Equation (5.3). The Standard Model distribution  $y_{SM}$  is compared against the alternative distribution  $y_{Alt}$  for every bin  $i$ . Since a Poisson distribution is expected, hence the resolution can be represented as  $\sqrt{y_{SM}}$ .

$$\chi^2 = \sum_{i=1}^{bins} \left( \frac{y_{SM,i} - y_{Alt,i}}{\sqrt{y_{SM,i}}} \right)^2 \quad (5.3)$$

A small  $\chi^2$  value implies equal distributions while a large value implies distinguishable distributions. For the two selected helicity values the associated helicity distribution should differ from the Standard Model distribution, thus a high  $\chi^2$  value is expected. In case of a low  $\chi^2$  value, the corresponding alternative helicity cannot be distinguished from the Standard Model helicity. Hence for the associated working point, a large region in the helicity  $(f_+, f_0)$  plane is considered to represent the Standard Model. Since the method to determine the W-boson helicity exploits the deviations between the different helicity points, the  $(f_+, f_0)$  region of indistinguishable helicity values around each point should be as small as possible. Such a large region can be due to bad reconstruction of the event topology or due to low number of remaining

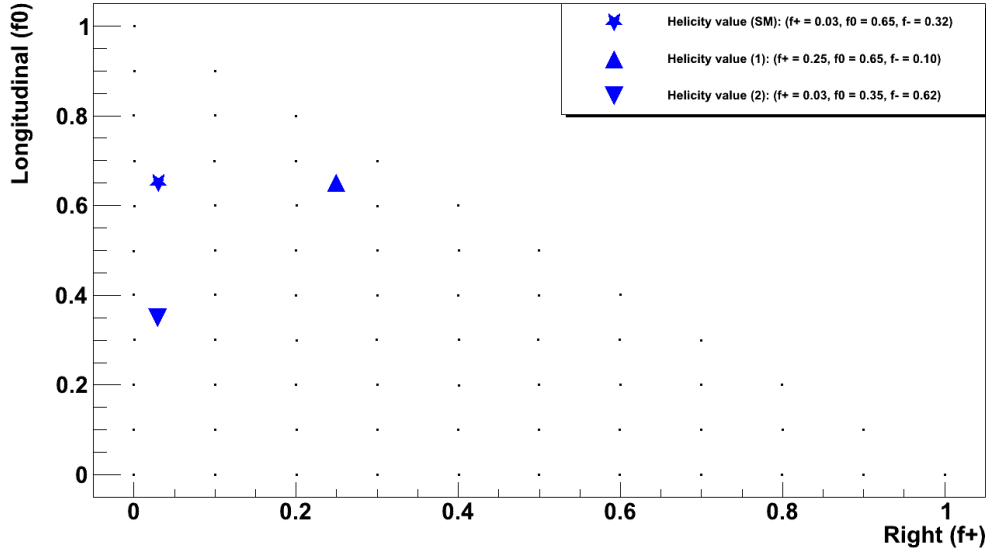


**Figure 5.9:** Helicity ( $f_+$ ,  $f_0$ ) plane containing the Standard Model helicity and the two helicity configurations used to determine the effect of b-tagging on the W-boson helicity measurement.

events after the application of b-tagging.

The obtained  $\chi^2$  values together with the remaining selected events for the different working points are given in Table 5.2. From this can be concluded that the Loose working point has the best balance between a relative high  $\chi^2$  value and enough remaining events to measure the W-boson helicities. Table 5.2 indicates a large increase between no applied b-tagging and a Loose working point b-tagging, but only a small increase for the Medium working point. Since the number of remaining selected events for the Medium working point is very low, this analysis will use a Loose working point b-tagging. The signal over background ratio represents the number of semi-muonic  $t\bar{t}$  events compared to the total number of background events. As expected this value increases with a more efficient applied b-tagging working point.

The effect of an applied b-tag on the helicity distribution can be found in Figures 5.10, which represents the distribution in the case of a Loose and a Medium working point. These distributions should be compared with Figure 5.1, the helicity distribution without applied b-tag constraint. It can be concluded that the application of a Loose b-tag significantly reduces the W + jets background while the effect of the Medium b-tag is less visible. This observation is confirmed in Table 5.3 which gives, for different b-tagging

	$\chi^2_{SM,1}$	$\chi^2_{SM,2}$	# events	Signal/Background
<b>No bTag</b>	1.59	1.68	274	0.811
<b>Loose bTag</b>	2.46	2.75	103	1.901
<b>Medium bTag</b>	2.66	2.78	59	3.301

**Table 5.2:**  $\chi^2$  values, number of selected events and signal over background ratio for the different b-tagging working points. For this thesis the Loose b-tag working point is optimal.

working points, the number of events for the used simulation samples.

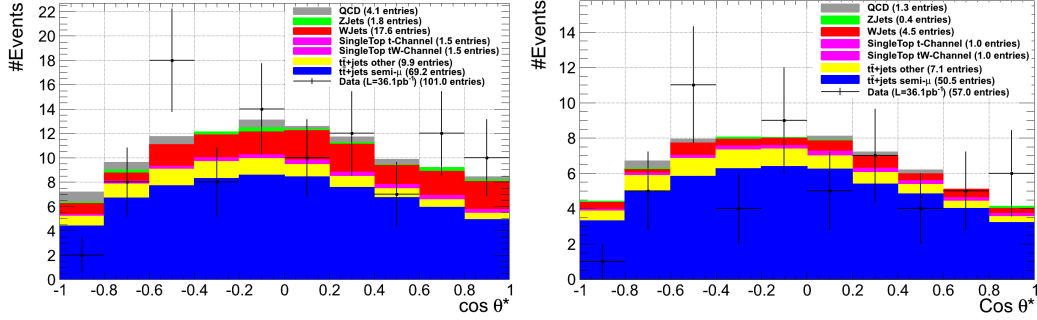


**Figure 5.10:** Helicity distribution with applied Loose (a) and Medium (b) working point b-tagging algorithm.

Also Figure 5.11 shows the effect of the application of b-tagging on the leptonic b-quark. It represents, just as Figure 5.7, the difference between the  $\cos \theta^*$  value after reconstruction with the value obtained on generator level for semi-muonic  $t\bar{t}$  events. It clearly shows a better reconstruction in the case of the Loose b-tag, which is also reflected in the associated resolution values. This resolution is again determined with a Gaussian fit onto the limited  $\Delta \cos \theta^*$  of  $-0.3$  and  $0.3$  and shows a significant enhancement between no and loose working point applied b-tagging.

With the use of b-tagging on the b-quark associated with the leptonic decaying W-boson, the reconstruction of the  $\cos \theta^*$  distribution will be much more efficient. The deviations on the helicity distribution originating from the reconstruction of the different particles present in the studied event will significantly change, as shown in Figure 5.12. This can be compared with Figure 5.6 which represents the same contributions, only without any ap-

	No b-tag	Loose b-tag	Medium b-tag
$t\bar{t}$ semi- $\mu$	132.7	69.2	50.5
$t\bar{t}$ other	19.8	9.9	7.1
single t (tW Channel)	3.9	1.5	1.0
single t (t Channel)	4.0	1.5	1.0
Z + jets	12.4	1.8	0.4
W + jets	104.5	17.6	4.5
QCD	19.0	4.1	1.3
<b>Total Simulation</b>	<b>296.3</b>	<b>105.6</b>	<b>65.8</b>
<b>Data</b>	<b>272.0</b>	<b>101.0</b>	<b>57.0</b>

**Table 5.3:** Number of events for the different working points. The events in the simulated sample have been rescaled down to the data luminosity of  $36.1389 \text{ pb}^{-1}$ .

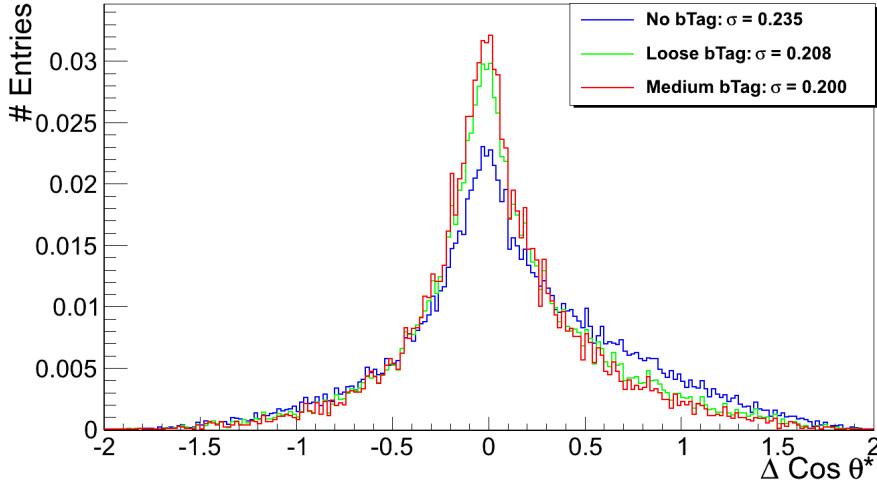


**Figure 5.11:** Comparison of  $\cos \theta^*$  value obtained on generator level with the value after reconstruction for all semi-muonic  $t\bar{t}$  events. A Gaussian fit onto the limited  $\Delta \cos \theta^*$  range was applied to obtain the resolution  $\sigma$ .

plied b-tag. Hence the use of a Loose working point b-tag improves the reconstructed  $\cos \theta^*$  distribution and reduces the impact of the individual particle reconstruction efficiency.

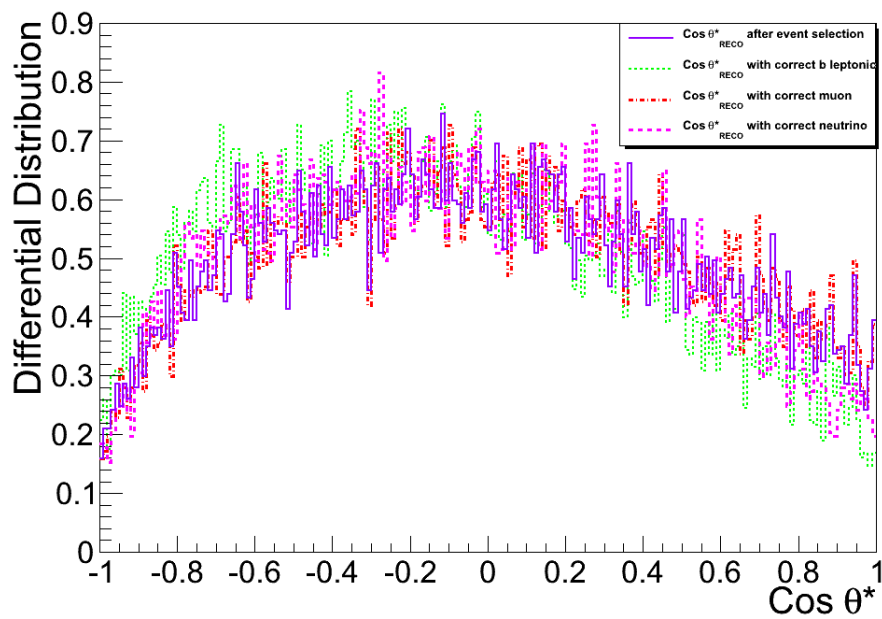


**Figure 5.12:** Effect of reconstruction on semi-muonic  $t\bar{t}$  helicity distribution with Loose working point b-tagging applied. Distribution for complete event reconstruction (purple) and for reconstruction with one particle obtained on parton level is shown, respectively the muon (dashed red), neutrino (dashed pink) and b-quark (dashed green).

# Chapter 6

## Measurement on 2010 data

In this analysis, a reweighting algorithm is used for each event by comparing the theoretical helicity distribution on generator level for the Standard Model and the alternative helicity values. In order to obtain an efficient reconstruction, a track counting high efficiency b-tagging algorithm with Loose working point was applied onto the b-quark originating from the leptonic decaying top quark.

This chapter describes the measurement of the W-boson helicity and the influence of systematic uncertainties on this measurement.

### 6.1 Helicity Measurement

The W-boson helicity values are measured using a minimal  $\chi^2$  algorithm, given in Equation (6.1). The data distribution  $y_{Data}$  is compared against the alternative distribution  $y_{Alt}$  for all the bins  $i$ . Since a Poisson distribution is expected, the resolution is represented by  $\sqrt{y_{Data}}$ . It should be noted that the  $\chi^2$  method is dependent of the corresponding helicities  $f_+$  and  $f_0$ .

$$\chi^2(f_+, f_0) = \sum_{i=1}^{bins} \frac{(y_{alt,i} - y_{Data,i})^2}{y_{Data,i}^2} \quad (6.1)$$

This algorithm compares the helicity distribution of the data sample with the simulated distributions obtained for the different alternative helicities. For each helicity configuration a probability value or p-value to correspond with the data distribution is calculated. The algorithm is normalized such that a minimal  $\chi^2$  value results in a p-value equal to 1, making it possible to compare different measurements. The data distribution against which all alternative simulated distributions are compared is given in Figure 6.1.

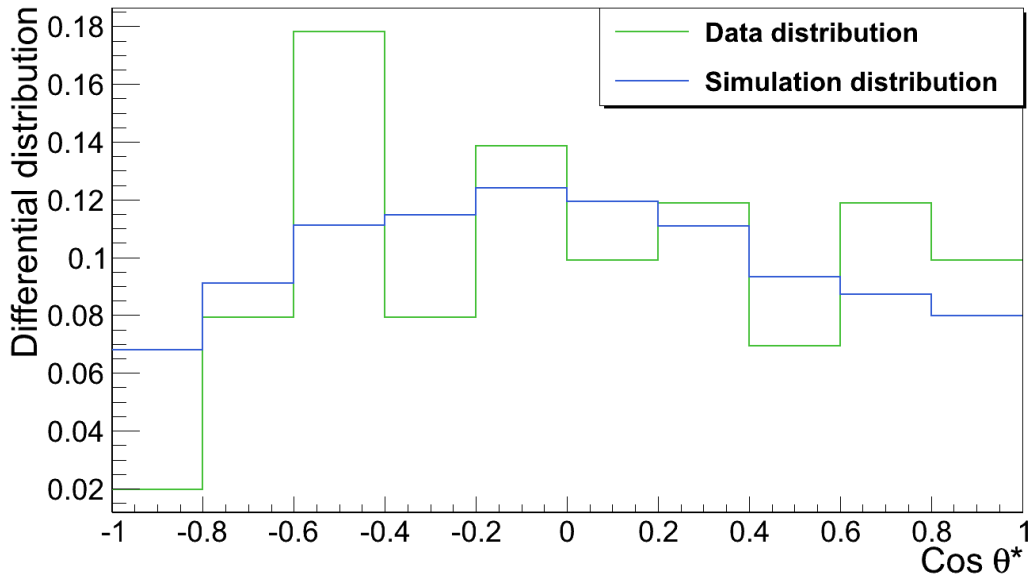
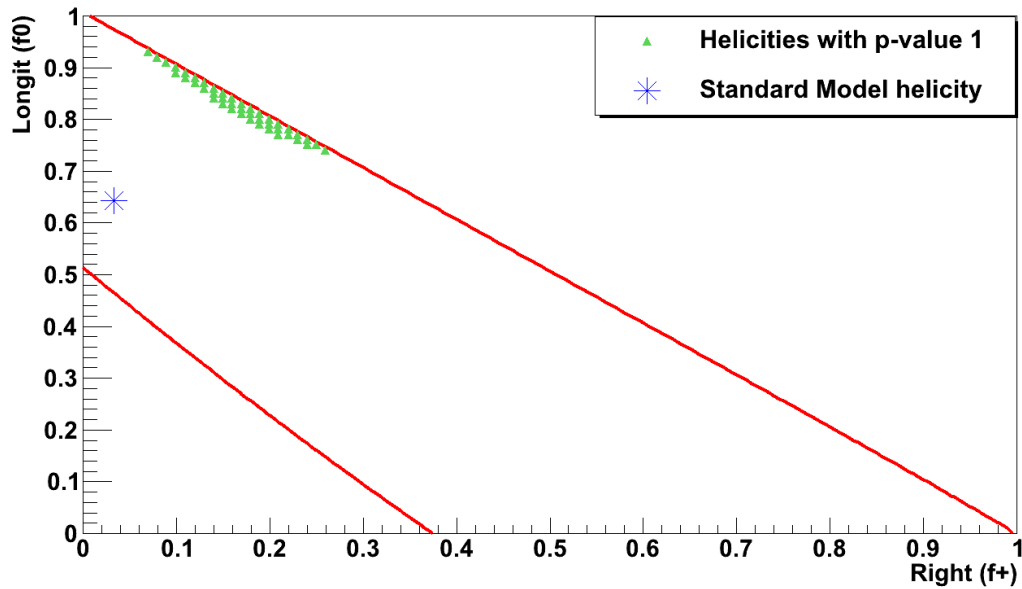


**Figure 6.1:** Helicity distribution for the data sample compared to the simulated distribution obtained for the Standard Model helicity values.

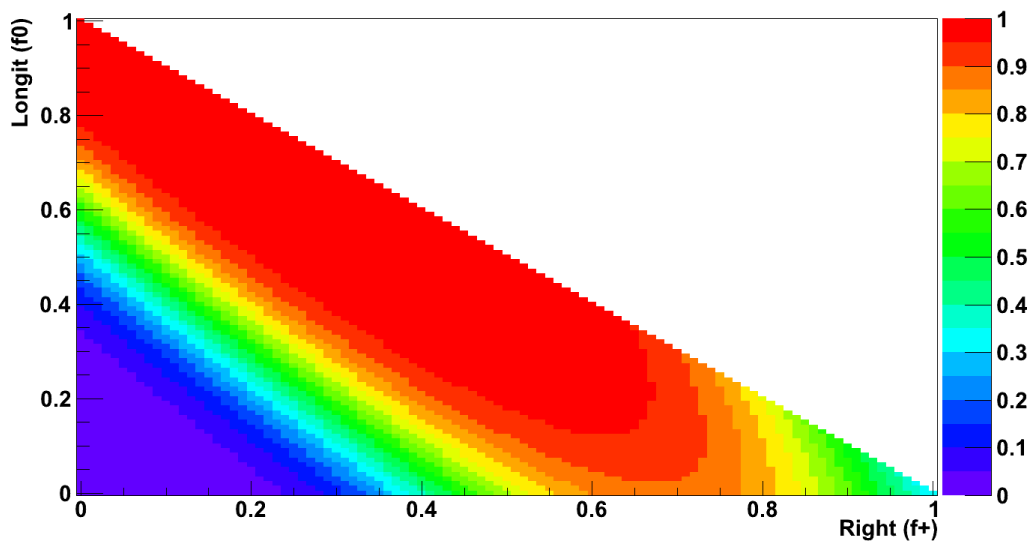
Figure 6.1 indicates the difficulties present to compare the data distribution with the simulated distribution. Due to low statistics, data sample only contains 36 pb<sup>1</sup> collected luminosity, the data distribution has no clear distribution shape.

This is represented in the obtained result for the minimal  $\chi^2$  algorithm. Figure 6.2(a) gives the 68 % Confidence Level, indicating that helicity values which lie in these contours are at 1 standard deviation of the best fitted result. The 95 % Confidence Level contour, at 2 standard deviations, was excluded since it consisted of the entire helicity plane due to the restricted data luminosity. With the current available statistics the obtained contours cannot be used to conclude whether the W-boson helicity measurement for data deviates from the Standard Model, only that the measurement is in agreement with the Standard Model prediction.

Figure 6.2(b) shows the full p-value distribution for the different alternative helicity values. From this is clearly visible that even the contour with p-values between 1 and 0.95, hence excellent agreement with data distribution, comprise almost half of the helicity plane.



(a)



(b)

**Figure 6.2:** a) Helicity configurations with maximum p-value together with the calculated 68 % Confidence Level. b) P-value distribution for different helicity configurations. Both results are in agreement with the Standard Model.

## 6.2 Systematic Uncertainties

Here the effect of systematic uncertainties on the W-boson helicity measurement is studied. With the current available data reflecting an integrated luminosity of  $36 \text{ pb}^{-1}$ , the uncertainties on the measurement are dominated by statistics, as was shown in Figures 6.2. Still the influence of systematic uncertainties need to be considered to understand the possible effect when the integrated luminosity will increase.

In this thesis the effect of systematic uncertainties on the measurement will be analyzed by comparing the Standard Model helicity distribution for simulation samples with the helicity distributions for different helicity values obtained with the same simulation samples. As for the measurement, the minimal  $\chi^2$  algorithm will be used.

Therefore the luminosity for which the simulation samples are scaled plays an important role. As explained before, when data is compared against simulation, the total simulation is scaled towards the data luminosity in order to obtain an agreement between data and simulation. When simulation is compared against simulation, the scaled luminosity is determined by the lowest luminosity present in the total simulation sample. By using this luminosity, instead of the data luminosity, the statistical uncertainty is reduced such that the systematic effect can be studied more accurate.

### 6.2.1 Variation of Jet Energy Scale

In order to estimate the influence on the measurement due to imperfect knowledge of the jet energy scale, the jet energy scale is altered with 5 % for the semi-muonic  $t\bar{t}$  sample. This value is really conservative and will be extrapolated towards the more realistic 2 % deviation. To ensure enough statistics, the semi-muonic  $t\bar{t}$  sample will be scaled towards the luminosity of the full simulated sample of top quark pair events, namely  $7800 \text{ pb}^{-1}$ .

To observe the influence of the jet energy scale on the semi-muonic  $t\bar{t}$  simulation, first this sample is compared with itself without an applied deviation of the jet energy scale. Hence a perfect match with the obtained Standard Model helicity values,  $(f_+, f_0) = (0.033, 0.642)$ , is expected.

The result obtained for the semi-muonic  $t\bar{t}$  sample is given in equation (6.2), which shows an excellent agreement with the Standard Model values. Due to the high luminosity for semi-muonic  $t\bar{t}$ , the influence of statistical uncertainties is very small.

$$(f_+, f_0) = (0.035, 0.64) \pm (0.005, 0.01) \quad (6.2)$$

The influence of the jet energy scale systematics on the helicity measurement is given in Equation (6.3). This shows as good as no effect on the right-handed helicity and only a small effect on the longitudinal helicity. An increase of the jet energy scale raises the best-fitted result in the helicity  $(f_+, f_0)$  plane while a decrease lowers the best-fitted result, shown respectively in Equation (6.3a) and (6.3b).

$$(f_+, f_0) = (0.04, 0.745) \pm (0.005, 0.01) \quad (6.3a)$$

$$(f_+, f_0) = (0.04, 0.575) \pm (0.005, 0.01) \quad (6.3b)$$

From Equation (6.3) is visible that the systematic influence of the jet energy scale on the right-handed helicity is equal with the statistical uncertainty while the systematic uncertainty on the longitudinal helicity is about 8 times larger than the statistical uncertainty. In Table 6.1 it is shown that for the more realistic 2 % variation in jet energy scale the rate between the systematic and statistical uncertainty is reduced to 3.4.

Table 6.1 summarizes the obtained results and gives the procentual influence of the overall variation of the jet energy scale. Against the current statistical uncertainty on the data measurement, this influence is negligible. But compared with the statistical uncertainty on simulated semi-muonic  $t\bar{t}$  events the jet energy scale is larger than the statistical uncertainty.

	$\Delta f_+$ (%)	$\Delta f_0$ (%)
$\pm 5$ % Jet Energy Scale	0.5	8.5
$\pm 2$ % Jet Energy Scale	0.2	3.4

**Table 6.1:** Procentual deviation on right-handed and longitudinal helicity after differentiating the jet energy scale with 5 %. The values for 2 % jet energy scale difference has been obtained by extrapolation.

## 6.2.2 Variation of W Cross Section

The influence of the uncertainty on the determination of the theoretical cross section of the  $W + \text{jets}$  background can have a large effect on the measurement. Especially since the  $W + \text{jets}$  sample has the largest background contribution of all background samples. The luminosity of this sample is

only about  $350 \text{ pb}^{-1}$ , hence statistical uncertainties will be more important than for the previous systematics, the jet energy scale.

When the combined semi-muonic  $t\bar{t}$  and  $W + \text{jets}$  samples are compared to each other with the minimal  $\chi^2$  method, the result shown in Equation (6.4) are obtained. The results have been scaled to only  $300 \text{ pb}^{-1}$ , to account for the decrease with 30 %.

$$(f_+, f_0) = (0.035, 0.64) \pm (0.035, 0.07) \quad (6.4)$$

Due to the restricted statistics, this result is less accurate than the result obtained for the semi-muonic  $t\bar{t}$  sample only. Hence the influence of the  $W + \text{jets}$  cross section on the measurement will be less precise to observe.

The results obtained for the variation of the cross section can be found in Equation (6.5), respectively Equation (6.5a) for the 30 % increase of the cross section and Equation (6.5b) for the decrease in cross section.

$$(f_+, f_0) = (0.045, 0.685) \pm (0.035, 0.075) \quad (6.5a)$$

$$(f_+, f_0) = (0.025, 0.595) \pm (0.025, 0.065) \quad (6.5b)$$

Equation (6.5) indicates that in the case of the  $W + \text{jets}$  cross section variation the influence on both the right-handed and longitudinal helicity is negligible against the large systematic uncertainties. Still it is visible that the  $W + \text{jets}$  systematic has an influence comparable with the jet energy scale systematic. Hence for further increasing luminosity this systematic can become more important.

The influence of the  $W + \text{jets}$  cross section has been summarized in Table 6.2.

	$\Delta f_+$ (%)	$\Delta f_0$ (%)
$\pm 30 \text{ W +jets Cross section}$	1	4.5

**Table 6.2:** Influence of the  $W + \text{jets}$  cross section on the W-boson helicity measurement.

### 6.2.3 Effect of Background Processes

The influence of the simulation samples other than the semi-muonic  $t\bar{t}$  samples is expected to be negligible since these samples contain no information

about the  $W$ -boson helicities. Hence any observed influence would indicate a systematic effect on the measurement induced by the background.

As explained above, the used scaled luminosity should be the lowest luminosity available in the complete simulation sample. Hence the QCD luminosity of  $160 \text{ pb}^{-1}$  needs to be used. The best-fitted helicity result for the semi-muonic  $t\bar{t}$  sample only scaled to the QCD luminosity is given in Equation (6.6).

$$(f_+, f_0) = (0.07, 0.61) \pm (0.07, 0.14) \quad (6.6)$$

The restriction due to the small statistics is clearly visible in Equation (6.6). The statistical uncertainty is about 7 times larger for the semi-muonic  $t\bar{t}$  luminosity. Hence the observation of systematic influences will become very difficult. The result for all the simulation samples scaled to the QCD luminosity is given in Equation (6.7).

$$(f_+, f_0) = (0.045, 0.635) \pm (0.045, 0.105) \quad (6.7)$$

Equation (6.7) indicates that the statistical uncertainty is significantly larger than the systematic uncertainty, making it impossible to conclude about possible influences of the background.

In order to obtain an indication of the importance of the background systematic the previous measurements were repeated onto the entire simulation sample, with the QCD sample excluded. Hence the lowest luminosity present in the entire simulation sample corresponds to the  $W + \text{jets}$  luminosity of about  $360 \text{ pb}^{-1}$ . The exclusion of the QCD sample significantly increases the statistics, as will be shown in the following results.

Equation (6.8) represents the best-fitted  $W$ -boson helicity measurement for the semi-muonic  $t\bar{t}$  simulation sample scaled to the  $W + \text{jets}$  luminosity. Compared with the previous result, QCD sample included, the statistical uncertainty is about halve.

$$(f_+, f_0) = (0.03, 0.64) \pm (0.03, 0.06) \quad (6.8)$$

The results obtained for the simulation sample with the QCD sample excluded are given in Equation (6.9).

$$(f_+, f_0) = (0.035, 0.64) \pm (0.035, 0.07) \quad (6.9)$$

As expected, Equation (6.9) indicates a negligible contribution from the background processes onto the  $W$ -boson helicity measurement. For the right-handed helicity a variation of 0.5 % is observed which is not significant compared with the statistical uncertainty of 3.5 %. The left-handed helicity has

no visible influence from the background systematic.

Figure 6.3 represents the obtained regions with best-fitted values in the case the QCD luminosity is used as scaled luminosity and in the case the W + jets luminosity is used. It clearly shows the difference in width of the best-fitted region due to the difference in luminosity. As expected the best-fitted region is not shifted in the helicity ( $f_+$ ,  $f_0$ ) region, but the width has changed.

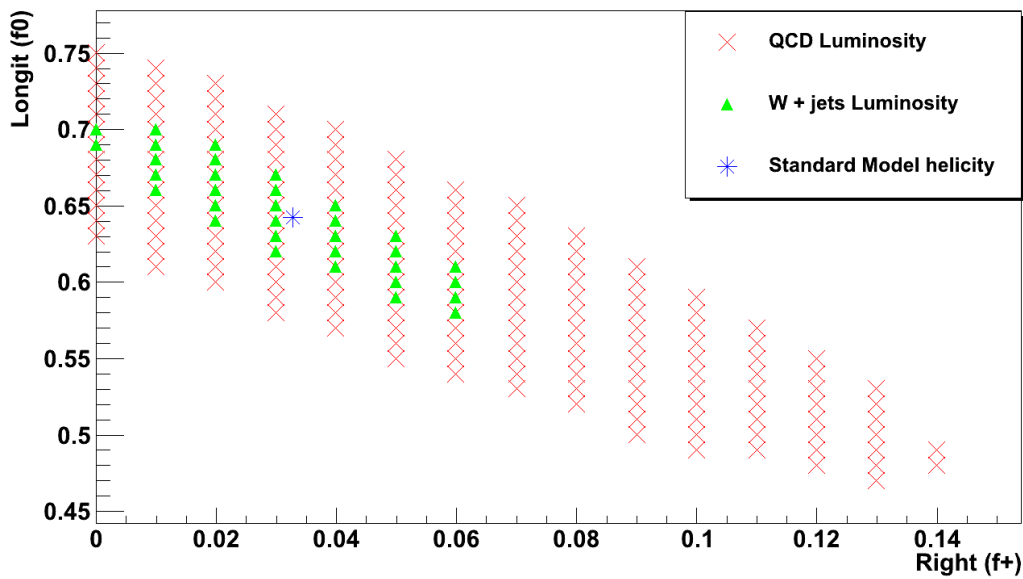


**Figure 6.3:** Comparison between the obtained best-fitted values for QCD luminosity (red cross) and for W + jets luminosity (green triangle).

# Chapter 7

## Conclusions and Outlook

In this thesis a measurement of W-boson helicities was performed using data collected in 2010 with the Compact Muon Solenoid experiment. The measured jets are matched to the underlying quarks with a minimal  $\chi^2$  jet-quark matching algorithm with top quark and W-boson mass constraints. The neutrino kinematics were reconstructed by assuming a massless neutrino such that a quadratic equation with W-boson mass constraint can be used. In order to obtain simulated helicity distributions to compare against the data distribution, a weighting algorithm has been applied. This algorithm compares the helicity distribution on generator level for the Standard Model helicities against the distribution on generator level for the alternative helicity. The generator level distribution has to be used to avoid influences from the event selection and reconstruction method. A track counting high efficiency b-tagging algorithm with Loose working point has been applied onto the b-quark of the leptonic decaying top quark. Since this quark is not comprised in the jet-quark matching algorithm, the b-tag will increase the reconstruction efficiency.

An efficient reconstruction of this b-quark and the neutrino is essential for the measurement of the W-boson helicity since the observed decay angle  $\theta^*$  is defined as the angle between the lepton in the W-boson restframe and the W-boson in the top restframe. Hence accurate kinematics for these particles are necessary to rebuild the event topology.

A similar measurement has never been performed at the CMS detector, however the Tevatron has accurately studied this subject, as explained in [46, 47]. The most recent Tevatron result is given in Equation (7.1), for which  $5.4 \text{ fb}^{-1}$  of  $p\bar{p}$  collision data has been used. In order to obtain enough statistics, the lepton + jets and dilepton channels for electrons and muons have been combined.

$$f_0 = 0.669 \pm 0.078(stat) \pm 0.065(syst) \quad (7.1a)$$

$$f_+ = 0.023 \pm 0.041(stat) \pm 0.034(syst) \quad (7.1b)$$

Since the amount of data which can be collected with the Large Hadron Collider is larger compared to Tevatron, the LHC will soon improve the accuracy obtained on the measurement. For this thesis only 2010 data was used, hence a luminosity of  $36.1 \text{ pb}^{-1}$ . Therefore the current CMS results, shown in Equation (7.2), are less accurate.

$$f_0 = 0.835 \pm 0.425(stat) \pm 0.045(syst) \quad (7.2a)$$

$$f_+ = 0.165 \pm 0.495(stat) \pm 0.01(syst) \quad (7.2b)$$

Equation (7.2) indicates a lower systematic uncertainty than the Tevatron result, but these values cannot be compared. Since Tevatron has more statistics the systematic uncertainty becomes important, hence various influences has been studied with much detail. In this thesis only a basic, preliminary study of the systematics has been performed since the measurement is dominated by statistical uncertainty.

The current collected data of 2011 already exceeds the total collected amount of 2010. Since this was only made available for analysis in end May, it was practically impossible to use the 2011 data for this analysis. Therefore the analysis will be repeated in July on approximately  $1 \text{ fb}^{-1}$  available data, which will result in a more accurate result. Comparison against the Tevatron uncertainty band indicates that an integrated luminosity of  $2 \text{ fb}^{-1}$  at CMS is sufficient to compete with the Tevatron result on accuracy.

The performed analysis still has room for improvement, as was explained in Chapters 3, 4 and 5. It was mentioned that the reconstruction of the neutrino has a low efficiency and a large influence onto the helicity distribution. Also the event selection, currently Selection Version SelV4 has been used, can be optimized in order to increase the background contribution even further. The jet-quark matching algorithm described in this thesis will be changed into a Kinematic Fit algorithm. Also the used track counting high efficiency algorithm will be replaced with a Combined Secondary Vertex, once it has been commissioned on data.

The influence of the different aspects is very complex and can be considered

---

as individual analysis. Based on the work presented in this thesis, a *W Helicity and Wtb Couplings working group* formed in the CMS Collaboration. Hence for the continuation of the W-boson helicity analysis the different improvements on the analysis will be combined in order to obtain the most accurate result.

# Summary

In this thesis the measurement of the W-boson helicity of the W-boson was discussed. This measurement was performed with the Compact Muon Solenoid experiment at the Large Hadron Collider, located at Cern, Geneva. The Large Hadron Collider is the most energetic hadron collider of the world and is designed to collide protons at a centre-of-mass energy of 14 TeV. Since 30 March 2010 proton-proton collisions are taking place with a beam energy of 3.5 TeV, hence half of the design energy. Between 30 March and 31 October an integrated luminosity of  $36.1 \text{ pb}^{-1}$  was collected and was used for this analysis.

The W-boson helicity is measured in top quark interactions since top quarks decay before hadronization due to their high mass. Hence top quarks are the only quarks which can be studied as free quarks and their spin information is not lost. Since the top quark decays almost exclusively in a W-boson and a bottom quark, the spin of the top quark restricts the possible spin configurations of the W-boson and the bottom quark. The obtained helicity of the W-boson can be measured by the angular distribution between its decay products, two light quarks or a lepton and the corresponding neutrino. This distribution has a specific shape for the different helicities, namely right-handed, longitudinal or left-handed.

The decay angle  $\theta^*$ , studied in this analysis, is defined as the angle between the down-type fermion in the W-boson restframe and the W-boson in the top quark restframe. In this analysis is chosen to only study semi-muonic  $t\bar{t}$  events, hence events for which one W-boson decays in two quarks and the other in a muon and muon-neutrino. For this configuration the signal can best be distinguished from the large background, due to the presence of the muon.

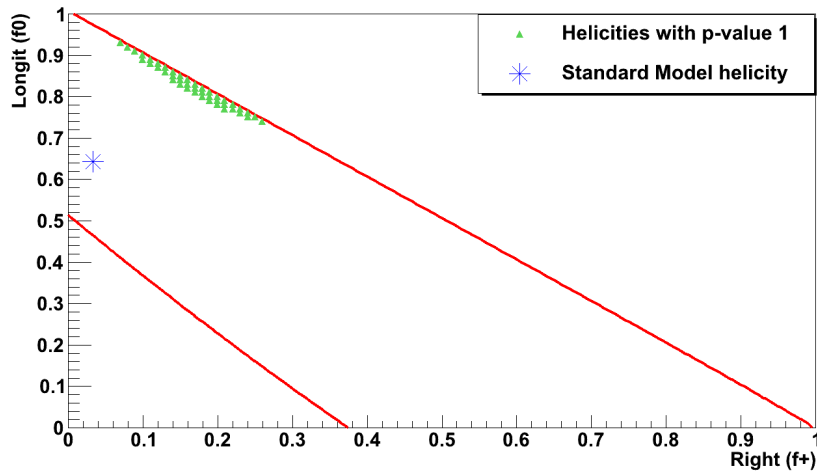
In order to reboost particles in their restframes, the kinematics should be determined accurately. In the CMS experiment this is done with specific methods based on the different signals of particles in the subdetectors. These measured signals are then matched to the particles in the event, for the present jets this is done with a  $\chi^2$  jet-quark matching algorithm. The iden-

tification of the bottom quark, originating from the leptonic decaying top quark is improved by a b-tagging algorithm. Such an algorithm exploits the characteristic property of the bottom quark that it decays into B-hadrons during fragmentation. Hence a secondary vertex can be observed in the CMS detector.

The actual measurement of the W-boson helicity is performed by comparing the helicity distribution obtained for data with the distribution obtained for alternative helicities. The helicity value which has the best match with the data distribution is considered as the measured helicity of the W-boson.

With the current available data, the statistical uncertainty is larger than the influence of systematic uncertainties. This will change in the following months and years when LHC continues collecting data.

The obtained result is represent in the following figure as a 68 % Confidence Level contour in the helicity plane ( $f_+$ ,  $f_0$ ), restricted by the relation  $f_+ + f_0 + f_- = 1$ .



Measuring the W-helicity is essential since it can indicate towards phenomena beyond the Standard Model. Due to the large top quark mass, this quark is very sensitive to influences beyond the Standard Model.

In the Standard Model it is expected to only observe left-handed and longitudinal helicities, but not right-handed helicities. Hence any observed deviation from the predicted Standard Model fractions would indicate that the weak charged current interaction, responsible for the decay of the top quark, is influenced by new physics phenomena.

With the current available data no deviation has been observed and the measured result is in agreement with the Standard Model.

# Samenvatting

In deze thesis wordt de meting van de helichiteit van het W-boson besproken. Deze meting is uitgevoerd met het Compact Muon Solenoid experiment van de Large Hadron Collider te CERN, Geneve. De Large Hadron Collider is de meest energetische hadron botser ter wereld en is ontworpen om protonen te laten botsen bij een energie van 14 TeV. Sinds 30 maart 2010 is de LHC operationeel en worden botsingen waargenomen bij een energie van 7 TeV. Tussen 30 maart 2010 en 31 oktober 2010 werd een geïntegreerde luminositeit van  $36.1 \text{ pb}^{-1}$  opgenomen en beschikbaar gesteld voor analyse.

Het is op deze hoeveelheid proton-proton botsingen dat de besproken analyse werd uitgevoerd. De W-boson helichiteit wordt gemeten in top quark interacties aangezien deze quarks door hun hoge massa vervallen voor ze hadroniseren. Hierdoor is het mogelijk om het top quark als een vrij quark te bestuderen en blijft de spin informatie van het verval intact. Omdat het top quark zo goed als altijd vervalft in een W-boson en een bottom quark legt de spin van het top quark beperkingen op de mogelijke spin configuraties van zijn vervalproducten. De bekomen helichiteit van het W-boson beperkt de hoekverdeling tussen zijn vervalproducten, twee quarks of een lepton en respectievelijk neutrino. De vervalhoek  $\theta^*$  bestudeerd in deze thesis is gedefinieerd als de hoek tussen het down-type fermion in het W-boson ruststelsel en het W-boson in het top quark ruststelsel.

Om een duidelijk signaal te kunnen bekomen is in deze thesis gekeken top quark gebeurtenissen waarbij een W-boson leptonisch vervalft, namelijk in een muon en muon-neutrino, en het andere W-boson hadronisch vervalft in twee quarks.

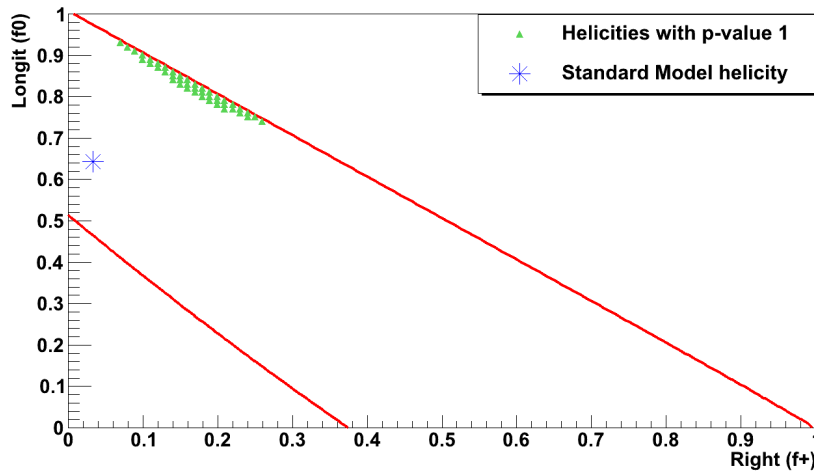
Om fysische deeltjes terug te boosten in hun ruststelsels, is het nodig om de kinematische eigenschappen accuraat te bepalen. Dit wordt gedaan met specifieke methoden in het CMS experiment waarbij rekening wordt gehouden met het signaal van verschillende deeltjes in specifieke subdetectoren. De bekomen signalen moeten dan gepaard worden met de deeltjes aanwezig in het bestudeerde event. In deze thesis wordt dit gedaan met behulp van een jet-quark matching algoritme. De identificatie van het bottom quark

horende bij het leptonisch vervallende top quark wordt verbeterd door het taggen of identificeren met een b-tagging algoritme. Zo'n algoritme gebruikt de eigenschap dat een bottom quark vervalt in B-hadronen tijdens de fragmentatie. Deze hadronen zullen aanleiding geven tot een extra vertex die kan waargenomen worden met de CMS detector.

De uiteindelijke meting van de heliceiteit van het W-boson wordt gedaan door de heliceiteitsverdeling bekomen voor data te vergelijken met alternatieve heliceiteiten. De heliceiteitswaarde die het beste overeenkomt met de data verdeling wordt voorgesteld als de bekomen heliceiteit voor het W-boson.

Met de huidige beschikbare data is de statistische onzekerheid veel belangrijker dan de systematische. Dit zal veranderen in de volgende maanden en jaren als meer data beschikbaar wordt.

Het bekomen resultaat is weergegeven in onderstaande figuur als een 68 % Confidence Level contour in de parameter ruimte van  $(f_+, f_0)$  rekening houdend met de relatie  $f_+ + f_0 + f_- = 1$ .



De meting van de heliceiteit van het W-boson is zeer belangrijk omdat het aanwijzingen kan geven voor nieuwe fysica fenomenen. Door de grote top quark massa is deze quark zeer gevoelig voor fysica fenomenen niet beschreven door het Standaard Model. In het Standaard Model is verwacht dat het W-boson een linkshandige en longitudinale heliceiteit heeft, maar de rechtshandige is sterk onderdrukt. Daarom zou een afwijking in het aantal W-bosonen met rechtshandige heliceiteit een indicatie zijn dat de zwakke geladen stroom interactie die verantwoordelijk is voor het verval van het top quark beïnvloedt is door nieuwe fysica.

Met de huidige beperkte data is geen afwijking gevonden en het bekomen resultaat is in overeenkomst met het Standaard Model.

# Bibliography

- [1] *Particle Data Group*,  
<http://pdg.lbl.gov/>.
- [2] <http://public.web.cern.ch/public/en/About/About-en.html>.
- [3] F. Mandl and G. Shaw, *Quantum Field Theory*, (1984) 358 p.
- [4] M. E. Peskin and D. V. Schroeder, *An Introduction to Quantum Field Theory*, (1995) 815 p.
- [5] F. Englert and R. Brout, *Phys. Rev. Lett.* **13** (1964) 321 – 322.
- [6] P. W. Higgs, *Phys. Rev. Lett.* **13** (1964) 508 – 509.
- [7] M. Gomez-Bock et al., *Concepts of Electroweak Symmetry Breaking and Higgs Physics*, arXiv:0712.2419v1 [hep-ph] (2007).
- [8] S. Martin, *A Supersymmetry primer*, arXiv:hep-ph/9709356v5 (1997).
- [9] <http://public.web.cern.ch/public/en/Science/Science-en.html>.
- [10] M. Kobayashi, T. Maskawa, *CP-Violation in the Renormalizable Theory of Weak Interaction*, *Process of Theoretical Physics*, Vol 49, No.2, February 1973.
- [11] *The Fermilab Tevatron collider*,  
<http://www-bdnew.fnal.gov/tevatron/>.
- [12] CDF and D0 Collaboration, *Combination of CDF and D0 Results on the Mass of the Top Quark*, arxiv:1007.3178.
- [13] N. Kidonakis, *Top Quark cross sections and differential distributions*.
- [14] K. Nakamura et al. (2010), *Review of Particle Physics: The CKM Quark-Mixing Matrix*, *Journal of Physics G* 37 (075021): 150.

- 
- [15] G.L.Kane, G.A.Ladinsky and C.P.Yuan, *Using the top quark for testing standard-model polarization and CP predictions*, Phys Rev D **45**, 124 (1992).
- [16] J.A. Aguilar-Saavedra et al., *Probing anomalous Wtb couplings in top pair decays*, arXiv:hep-ph/0605190v2 (2007).
- [17] <http://www-d0.fnal.gov/Run2Physics/WWW/results/final/TOP/T05C/T05C.htm>.
- [18] S.L. Glashow, J. Iliopoulos, L. Maiani, *Weak Interactions with Lepton-Hadron Symmetry*, Physical Review D **2**, 1285 (1970).
- [19] L. Wolfenstein, *Parametrization of the Kobayashi-Maskawa Matrix*. Physical Review Letters **51**, 1945 (1983).
- [20] *The Large Hadron Collider Project*,  
<http://lhc.web.cern.ch/lhc>.
- [21] Amos Breskin and Rüdiger Voss (editors), *The CERN Large Hadron Collider: Accelerator and Experiments*, 2008 JINST **3** S08001-S08007.
- [22] *The CMS Experiment*,  
<http://cms.cern.ch/>.
- [23] *The CMS Collaboration*, S. Chatrchyan *et al.*, 2008 JINST **3** S08004
- [24] *The ATLAS Experiment*,  
<http://atlas.web.cern.ch/>.
- [25] *The ALICE Experiment*,  
<http://aliceinfo.cern.ch/>.
- [26] *The LHC-b Experiment*,  
<http://lhcb.web.cern.ch/>.
- [27] *The TOTEM Experiment*,  
<http://totem.web.cern.ch/>.
- [28] *The LHC-f Experiment*,  
<http://www.stelab.nagoya-u.ac.jp/LHCf/>.
- [29] [http://dbserve.pnpi.spb.ru/hepd/activities/hep\\_next.html](http://dbserve.pnpi.spb.ru/hepd/activities/hep_next.html)
- [30] *The MadGraph Matrix Element Generator*,  
<http://madgraph.phys.ucl.ac.be/>.

- 
- [31] T. Sjöstrand, S. Mrenna and P. Skands, *PYTHIA 6.4 Physics and Manual*, ArXiv:hep-ph/0603175v2 (2006).
- [32] GEANT4 Collaboration, S. Agostinelli et al. *GEANT4: A simulation toolkit*, Nucl. Instrum. and Methods **A506** (2003) 250 – 303.
- [33] [https://twiki.cern.ch/twiki/bin/viewauth/CMS/PileupInformation#2010\\_Pileup\\_Scenarios](https://twiki.cern.ch/twiki/bin/viewauth/CMS/PileupInformation#2010_Pileup_Scenarios).
- [34] CMS Collaboration, *Commissioning of the Particle-Flow Reconstruction in Minimum-Bias and Jet Events from pp Collisions at 7 TeV*, CMS PAS **PFT-10-002** (2010).
- [35] M. Cacciari et al. (2008), *The anti- $k_t$  jet clustering algorithm*, arXiv:0802.1189v2 [hep-ph].
- [36] CMS Collaboration, *Performance of muon identification in pp collisions at  $\sqrt{s} = 7$  TeV*, CMS PAS **MUO-10-002** (2010).
- [37] R. Frühwirth, *Application of Kalman filtering to track and vertex fitting*, Nucl. Instrum. Meth. **A262** (1987) 444 – 450.
- [38] CMS Collaboration, *Track impact based b-tagging with CMS*, CMS **NOTE 2006/019** (2006).
- [39] October 2009 exercise  
<https://twiki.cern.ch/twiki/bin/view/CMS/OctoberX>.
- [40] CMS Collaboration, *Selection of Top-Like Events in the Dilepton and Lepton-plus-Jets Channel in Early 7 TeV Data*, CMS PAS **TOP-10-004** (2010).
- [41] CMS Collaboration, *Jet Energy Calibration and Transverse Momentum Resolution in CMS*, CMS **PAPER JME-10-011** (to be published).
- [42] F. Blekman et al., *Selection of  $t\bar{t}$  Candidates in the Lepton+Jets Channels*, CMS **Analysis Note 2010/297** (2010).
- [43] T. Chwalek et al., *Measurement of the  $t\bar{t}$  cross section in the electron+jets and the muon+jets channels*, CMS **Analysis Note 2010/310** (2011).
- [44] V. Blobel, *An unfolding method for high energy physics experiments*, arXiv:0208022v1 [hep-ex] (2002).

- 
- [45] CMS Collaboration, *Measurement of the Polarization of  $W$  Bosons with Large Transverse Momenta in  $W$ +Jets Events at the LHC*, arXiv:1104.3829v1 [hep-ex] (2011).
- [46] D0 Collaboration, *Measurement of the  $W$  boson helicity in top quark decays using  $5.4 \text{ fb}^{-1}$  of  $p\bar{p}$  collision data*, ArXiv:1011.6549v1 [hep-ex] (2010).
- [47] D0 Collaboration, *Model-independent measurement of the  $W$  boson helicity in top quark decays at D0*, D0 Note **5722-CONF** (2008).